A competitive disinhibitory network for robust optic flow processing in *Drosophila*

Mert Erginkaya[1], Tomás Cruz[1], Margarida Brotas[1,2], Kathrin Steck[3], Aljoscha Nern[4], Filipa Torrão[1], Nélia Varela[1], Davi Bock[5], Michael Reiser[4] and M Eugenia Chiappe[1,6,*]

[1] *Champalimaud Neuroscience Programme, Champalimaud Centre for the Unknown, Lisbon, Portugal*

[2] *CEDOC, iNOVA4Health, NOVA Medical School, Universidade Nova de Lisboa, Lisbon, Portugal*

[3] *Center for Teacher Education and School Research, Universität Leipzig, Leipzig, Germany*

[4] *Janelia Research Campus, Howard Hughes Medical Institute, Ashburn, VA*

[5] *University of Vermont College of Medicine, VT*

[6] *Lead contact*

*Correspondence should be addressed to eugenia.chiappe@neuro.fchampalimaud.org

Summary

Many animals rely on optic flow for navigation, using differences in eye image velocity to detect deviations from their intended direction of travel. However, asymmetries in image velocity between the eyes are often overshadowed by strong, symmetric translational optic flow during navigation. Yet, the brain efficiently extracts these asymmetries for course control. While optic flow sensitive-neurons have been found in many animal species, far less is known about the postsynaptic circuits that support such robust optic flow processing. In the fly *Drosophila melanogaster*, a group of neurons called the horizontal system (HS) are involved in course control during highspeed translation. To understand how HS cells facilitate robust optic flow processing, we identified central networks that connect to HS cells using full brain electron microscopy datasets. These networks comprise three layers: convergent inputs from different, optic flow-sensitive cells, a middle layer with reciprocal, and lateral inhibitory interactions among different interneuron classes, and divergent output projecting to both the ventral nerve cord (equivalent to the vertebrate spinal cord), and to deeper regions of the fly

brain. By combining two-photon optical imaging to monitor free calcium dynamics, manipulating GABA receptors and modeling, we found that lateral disinhibition between brain hemispheres enhance the selectivity to rotational visual flow at the output layer of the network. Moreover, asymmetric manipulations of interneurons and their descending outputs induce drifts during highspeed walking, confirming their contribution to steering control. Together, these findings highlight the importance of competitive disinhibition as a critical circuit mechanism for robust processing of optic flow, which likely influences course control and heading perception, both critical functions supporting navigation.

Keywords

Optic flow, self-motion estimation, Drosophila, recurrent inhibition, steering control, heading perception, navigation

Introduction

As we navigate through space, our senses are continuously bombarded with a variety of stimuli from the environment and our own movements. Even for seemingly straightforward binary information, such as determining if we are veering to the left or right, our brains must extract and process the relevant signals from all incoming inputs to reorient according to our goals. Sensorimotor circuits that combine feedforward excitation with lateral inhibition have frequently been associated with this type of binary categorization[1,2] and behavioral choice[3–5]. However, how inhibitory interactions transform sensory information into categorical signals for continuous movement control is poorly understood.

Many animals rely on coherent patterns of image velocity across the retina to navigate according to goals. These patterns result from the relative motion between the moving observer and the surrounding scene, commonly known as optic flow[6,7]. The specific optic flow experienced by the observer depends on the direction and speed of the eyes, head, and

body. Therefore, optic flow provides valuable information about gaze, heading and traveling directions, allowing for a comparison with the intended trajectories for course control. Indeed, optic flow-sensitive neurons, which poses large monocular receptive fields sensitive to different axes of movement[8–11] are found across the animal kingdom[12–17] and have been implicated in heading perception, and gaze and course control[18–23]. Additionally, optic-flow sensitive neurons integrate multimodal information to distinguish between self-generated and externally generated information[13,24–27]. However, for accurate extraction of self-motion information, binocular integration between the eyes is also necessary. While some lateral interactions within optic flow-sensitive neurons have been identified[17,28–31], the precise mechanisms through which postsynaptic circuits integrate bilateral optic flow information to disambiguate self-motion and contribute to goal-directed navigation remain largely unknown.

The fly *Drosophila melanogaster* offers a valuable opportunity to investigate the circuit mechanisms involved in processing optic flow robustly. With its impressive visually guided behaviors, versatile genetic toolkit, comprehensive brain electron microscopy datasets, and well-characterized populations of optic flow-sensitive neurons, *Drosophila* allows for a systematic identification, and precise dissection of these mechanisms. In *Drosophila*, optic flow-sensitive neurons called lobula plate tangential cells (LPTCs) are found in deep layers of the fly's optic lobe and project to premotor regions of the brain. Certain LPTCs, like the horizontal system (HS) cells and H2 cells are sensitive to horizontal optic flow[32–34]. They receive non-visual signals related to angular velocity, which enhance their selectivity to the fly's rotations during spontaneous walking[27,33]. HS and H2 cells can also drive rotations of the fly[27,33,35], implicating them in course control. Recent work has shown that HS cells play a significant role in steering an exploratory fly, particularly during high-speed walking[35,36], when optic flow is dominated by symmetric translational components, which may overshadow the asymmetric ones caused by the fly's unexpected rotations. Thus, investigating HS cells and

77 their postsynaptic pathways provides an opportunity to understand how the network process
78 optic flow robustly, even in situations with a low signal-to-noise ratio.

79 In this study, we conducted a systematic analysis of the structure and function of
80 synaptic partners of HS and H2 at their central axon terminals. Our findings revealed that HS
81 and H2 cells form a subnetwork comprising three layers, including an input layer of converging
82 LPTCs, a middle layer of several classes of GABAergic interneurons, and divergent outputs
83 projecting back to the lobula plate (feedback), to the ventral nerve cord (VNC, the insect
84 analogous of the vertebrate spinal cord), or to deeper premotor regions of the fly brain. The
85 inhibitory layer forms recurrent connections with LPTCs and provides lateral inhibition across
86 the two brain hemispheres. Using two-photon calcium imaging of the newly identified
87 interneurons along with manipulating GABA receptors and modeling, we found that a lateral
88 disinhibition motif enhances rotational sensitivity at the network's output layer, supporting
89 steering control in freely exploring flies. Overall, our study unveils the layered anatomical
90 structure of optic flow networks and their strong modulation by inhibitory feedback and
91 elucidates how feedforward excitation combined with lateral disinhibition enables robust
92 extraction of asymmetries in optic flow signals between the eyes to guide reorientation of a
93 roaming fly.

94 Results

95 A class of optic flow-sensitive descending neuron contributes to steering during high-
96 speed walking

97 Course deviations can be determined by analyzing the differences in the pattern of
98 optic flow between the fly's eyes using binocular integration. However, these differences vary
99 with the fly's walking speed. Even when the deviation from a straight course is the same, flies
100 moving at low versus high speed induce distinct optic flow patterns (**Fig. 1a**, colored
101 rectangles). At low walking speeds, asymmetries in the optic flow can be easily detected, but

102 at high speed, these asymmetries are largely reduced due to the prominent translational
103 components in the optic flow (**Fig. 1a**). We currently lack a complete understanding of how
104 the networks responsible for processing rotational optic flow estimate asymmetries that
105 remain consistent regardless of the fly speed, enabling reliable walking control.

106 The horizontal system cells (HS cells), whose receptive fields are predominately
107 monocular[32], play a role in steering, especially during high-speed walking[35,36]. Recent work
108 has shown that these cells interact laterally (across hemispheres) via gap junction coupling
109 through an unidentified interneuron[30], potentially improving the detection of asymmetric optic
110 flow. If these lateral interactions enhanced the detection of asymmetric optic flow, output
111 neurons from the HS network should display increased sensitivity to rotational optic flow and
112 binocular activity compared to HS cells.

113 To explore this idea, we compared the response properties of the only known
114 descending neuron postsynaptic to HS cells, DNp15[30,37] to those of HS cells concerning optic
115 flow (**Fig. 1b,c**). We conducted *in vivo*, 2-photon calcium imaging in immobilized flies within
116 the inferior posterior slope (IPS) region of the fly brain (**Fig. 1c,** see **Methods**) while presenting
117 binocular asymmetric horizontal motion (i.e., stimuli representing rotations along the yaw axis)
118 or binocular symmetric horizontal motion (i.e., stimuli representing translational-like
119 movement along the forward direction (**Supplementary Video 1,** "Front-to-back/Back-to-
120 front" and "Yaw left/right" stimuli, respectively). In addition, to identify binocular interactions,
121 we compare the binocular responses of HS and DNp15 cells to those induce by monocular
122 stimuli.

123 We found that DNp15 exhibited response profiles and velocity tuning to binocular
124 asymmetric optic flow like HS cells, likely due to their electrical coupling[37] (**Fig. 1-S1a-c,**
125 **Supplementary Video 2**). However, DNp15 activity was more influenced by binocular
126 interactions compared to HS cells and showed a small but detectable response to
127 contralateral back-to-front visual motion (**Fig. 1d, 1-S1c**), suggesting an increased selectivity

128 to rotational optic flow. To describe the relative selectivity of HS and DNp15 to rotational vs.
129 translational stimuli, we defined a qualitative parameter called the discrimination index, which
130 compares the magnitude of the responses of a cell to rotational vs translational stimuli (see
131 **Methods**, **Fig. 1-S1e**). Overall, DNp15 demonstrated enhanced selectivity to rotational stimuli
132 than translational-like stimuli, unlike HS cells (**Fig. 1d,e, 1-S1d,e**). Thus, the network
133 associated with HS cells seems well suited to robustly detect asymmetries in binocular optic
134 flow for course control.

135 To test this idea, we investigated the role of DNp15 in walking control. DNp15 is
136 thought to contribute to gaze stabilization[37] and directly projects to dorsal neuropiles within
137 the tectulum of the ventral nerve cord[38] (VNC, the insect analogous of the spinal cord). Gaze
138 control depends on head-body coordination and course control[39]. Thus, we directly tested the
139 impact of DNp15 silencing on steering (course control) during highspeed walking by
140 expressing the inward rectifying potassium channel Kir2.1 in different configurations and
141 observing the walking paths of exploratory flies[39]. We created flies with unperturbed activity
142 of DNp15 (controls, i.e., no expression of Kir2.1), with balanced silenced DNp15 (bilateral
143 expression of Kir2.1), and with asymmetry in the activity of DNp15 (unilateral expression of
144 Kir2.1) (**Fig. 1-S1f**, see **Methods**). Flies typically exhibit runs of high forward velocity or turns
145 of low forward velocity (body saccades) under these experimental conditions (**Fig. 1f**, see also
146 **Fig. 6a**). We evaluated course control by calculating path deviation per run bout, or by
147 examining any biases during body saccades (**Fig. 1f,g**, **Fig. 1-S1g**, see **Methods**). Flies with
148 both DNp15 silenced or with no silencing did not show any bias during body saccades or runs
149 (**Fig. 1f,g** and **Fig. 1-S1g**, none or both silenced DNp15). However, unilateral silencing of
150 DNp15 resulted in contralateral path deviation during runs (**Fig. 1f,g**), while no biases were
151 observed during body saccades (**Fig. 1-S1g**, left or right silenced DNp15). These findings
152 suggest that asymmetry in activity of left vs. right DNp15 leads to steering biases during
153 forward walking. Furthermore, the enhanced selectivity of DNp15 to rotational vs. translational

154 optic flow implies that these neurons could detect minor differences in optic flow across the
155 eyes, thereby contributing to steering at high forward speed. However, the specific circuits
156 and mechanisms responsible for conveying such selectivity supporting robust optic flow
157 processing in DNp15 remain unknown.

158 **HS, H2 and VS cells connect distinctively to two parallel central networks**

159 To uncover the circuit and mechanisms responsible for robust rotational optic flow
160 processing, we investigated the downstream central synaptic partners of well-characterized
161 rotational optic flow sensitive cells, such as HS, H2, and VS cells. We used a complete female
162 adult fly brain (FAFB) electron microscopy (EM) dataset[40] (**Fig. 1-S2a-b**, see **Methods**) to
163 map the location of chemical synapses at the axon terminals of these LPTCs. By manually
164 tracing and identifying pre and postsynaptic partners (**Fig. 1-S2c**, see **Methods** for tracing
165 strategy), we found that HS, H2 and VS cells establish both input and output synaptic sites,
166 revealing central modulation of axonal activity in HS, H2 and VS cells (**Fig. 1-S2c-d**). We also
167 observed that these cells form few strong connections and numerous weak connections with
168 their synaptic inputs and outputs (**Fig. 1-S3a,b**). These results were confirmed using two
169 additional EM datasets with semi-automatically reconstructed neurons, FlyWire[41] and
170 Hemibrain[42] (**Fig. 1-S2a,c,d, S3**, **Supplementary Table 1**). Hence, our manual tracing
171 approach effectively identified important synaptic partners of HS, VS, and H2 cells. We
172 defined neurons providing more than 10 synaptic inputs to or receiving more than 35 synaptic
173 outputs from LPTCs as strong synaptic partners (**Fig. 1-S2d**, black lines).

174 To analyze the central networks involving these LPTCs, we computed a connectivity
175 matrix among all identified strong partners in the FAFB dataset (**Fig**. **2-S1**, see **Methods**).
176 While the matrix displayed rather sparse connections with weak or no connections between
177 most neuron pairs, certain pairs exhibited strong unidirectional connections with hundreds of
178 synapses (**Fig. 2-S1**). We performed a hierarchical cluster analysis on the pairwise number

179 of synapses (**Fig. 2-S1**, see **Methods**), and identified three primary clusters: HS and VS cells
180 with the interneuron IVLPT8, and two clusters forming separate networks with HS and VS
181 cells (**Fig. 2-S1** and **2a**). Importantly, this network structure remains mostly unchanged by
182 thresholding (**Fig. 2-S2**).

183 The VS network demonstrated strong connections between VS and central
184 interneurons (**Fig. 2a**), with output pathways diverging into descending pathways, including
185 neck motor neurons, and descending neurons (DNs), and feedback pathways to the ocelli,
186 the secondary optical system of flies[43,44]. On the other hand, the H2-HS network exhibited
187 strong connections among central interneurons, H2 and HS cells, and the GABAergic
188 feedback CH cells[29,45,46] (**Fig. 2a**). Like the VS network, the outputs of the HS-H2 network
189 diverged, with a descending pathway defined by several DNs projecting to leg, neck, and
190 haltere neuropiles in the VNC[38,47], and an ascending pathway of interneurons projecting to the
191 lateral accessory lobes (LAL).

192 The VS connections represented only a small proportion of total connections within
193 the H2-HS network and vice versa (**Fig. 2b**). This suggests that both networks largely operate
194 independently from each other. Notably, the DNs of the HS-H2 network are different from
195 those of the VS network, pointing towards parallel operation. Two DN outputs of the HS-H2
196 network, DNa02 and DNp15 have been previously characterized (**Fig. 1**)[37,47]. These neurons
197 are sensitive to fly rotations (or their visual consequence) and contribute to steering. The LAL,
198 the other output region of the HS-H2 network, is a higher-order premotor area of the insect
199 brain, thought to contribute to steering[48,49]. Together, these findings strongly support the
200 involvement the HS-H2 network in steering control.

201 **Recurrent connections define the intermediate layer structure of both networks**

202 The two networks, though largely non-overlapping, converge at the level of LPTC cells,
203 connecting to a small set of interneurons within the intermediate layers of the networks (i.e.,

204 between LPTCs and their outputs). We identified five distinct classes of LPTC input cells within
205 these intermediate layers that provide specific, recurrent input to HS, H2 and VS cells, thereby
206 defining the structure of the two networks (**Fig. 2-S3a-c**). Three of the five classes are
207 collectively defined as lobula plate tangential cell recurrent neurons (LPTCrns), due to their
208 shared soma location and tract, indicative of a common developmental origin. We differentiate
209 them based on anatomical features (**Fig. 2-S3b-d**).

210 Crab LPTCrn cells (**cLPTCrn**), central components of the VS network (**Fig. 2b**), extend
211 prominent projections to both hemispheres of the PS and connect reciprocally with most VS
212 and HS cells (**Fig. 2c**). Bilateral LPTCrn cells (bLPTCrn) also project to both hemispheres of
213 the PS, but their contralateral projections are limited to the dorsal area of the PS (**Fig. 2-S3b**).
214 Unilateral LPTCrn cells (uLPTCrn) are prominent components of the H2-HS network (**Fig. 2b**).
215 They project to the ipsilateral side and exhibit strong reciprocal connections with HS, H2, and
216 VS1-2, and VS7,8 cells (**Fig. 2c**).

217 The remaining two LPTC input classes specifically connect to HS and H2 cells. The
218 first class involves bilateral inferior posterior slope neurons (bIPS, **Fig 2-S3b**), which receive
219 strong convergent projections from ipsilateral HS and contralateral H2 cells and send
220 projections to the contralateral HSN and HSE cells (**Fig. 2c**). Notably, the two contralateral
221 CH cells are the strongest downstream partners of bIPS, receiving over 450 synapses from
222 bIPS as their strongest input (**Fig. 2-S1**). This provides strong anatomical evidence for a
223 central feedback pathway within this network. The second class of interneurons selectively
224 connects to the contralateral H2 cells at their axon terminals (**Fig. 2c**), referred as H2 recurrent
225 neurons (H2rn) as they receive input back from contralateral H2 cells.

226 The primary brain regions that send information to the intermediate layers of the VS
227 and HS-H2 are the PS, gnathal ganglion (GNG), and optic lobes. Additionally, all five cell
228 types receive direct ascending input from the VNC (**Fig. 2-S3e, Fig. 3b**). Thus, the
229 intermediate layers may operate as both integrators and broadcasters: they likely integrate

230 multimodal signals to modulate the optic flow sensitive networks, and broadcast optic flow
231 signals to numerous regions of the fly's CNS. The recurrent connections between LPTCs and
232 different classes of LPTC input neurons in the central brain suggest that these interneurons
233 possess distinct optic flow sensitivities based on their LPTC inputs, integrate extraretinal
234 signals in addition to optic flow, broadcast modulatory signals from premotor centers, and
235 shape the optic flow sensitivity of output neurons. Different sets of central interneurons within
236 the intermediate layers of the two networks may contribute in different visual-motor contexts.
237 In the following sessions, we focus on the functional properties of neurons within the different
238 layers of the HS-H2 network, and how optic flow signals are transformed to enhance DNp15's
239 selectivity to horizontal optic flow compared to HS cells.

240 **The H2-HS network exhibit responses to optic flow that are not entirely predicted by**
241 **their LPTC inputs**

242 To understand how the enhanced selectivity to rotational optic flow in DNp15 emerges
243 from the structure of the HS-H2 network, we characterized the optic flow responses of the
244 intermediate layer of the H2-HS network, which connect to DNp15 (**Fig. 2-S3f, Fig. 3a**). To
245 achieve cell-type-specific genetic access, we used traced EM skeletons to identify neurons in
246 transgenic line libraries (see **Methods, Fig. 3-S1a**). In vivo, neural recordings were conducted
247 under non-behaving conditions, focusing specifically on optic flow processing while minimizing
248 the potential impact of non-visual signals present in both LPTCs[25,27,33,50,51] and the network's
249 interneurons (**Fig. 3b**). We characterized neural responses to various patterns of optic flow
250 (**Supplementary Video 1**) by measuring calcium dynamics at axon terminals (e.g., **Fig. 3c**,
251 see **Methods** for choice of calcium indicators).

252 bIPS, uLPTCrn, and H2rn cells displayed responses to horizontal optic flow and
253 velocity tuning that showed similarities and differences compared to their inputs HS and H2
254 cells, (**Fig. 3d, Fig. 3-S2, Supplementary Video 2)**. First, uLPTCrn cells, which receive direct

255 input from VS (**Fig. 2c**), exhibited minimal or negative calcium signals to pitch and roll optic
256 flow, which would be expected to excite their presynaptic inputs from VS cells (**Fig. 3-S2a**).
257 Second, each class of interneurons displayed characteristic velocity tuning. While uLPTCrns
258 are more sensitive to slower than faster speeds, bIPS exhibit larger responses to intermediate
259 speeds, and H2rns are more sensitive to faster than slower speeds, in contrast to their
260 presynaptic H2 cells. These results suggest that cell autonomous properties or additional
261 inputs to these interneurons modulate visual responses of uLPTCrns and H2rns, either
262 through direct connections from other optic lobe neurons, or indirectly through inputs from the
263 central brain (**Fig. 3b**).

264 Further evidence for network-based modulation of visual inputs came from the
265 analysis of the responses of interneurons to monocular stimuli. bIPS and uLPTCrn cells
266 receive converging inputs from ipsilateral HS and contralateral H2 neurons (**Fig. 3a**), which
267 respond to front-to-back (FTB) and back-to-front (BTF) monocular motion, respectively (**Fig.**
268 **3-S2c**). Accordingly, one would expect both cell types to respond to ipsilateral progressive
269 and contralateral regressive stimuli. However, while both cell types responded to progressive
270 stimuli, they showed minimal responses to contralateral regressive motion (**Fig. 3-S2c**), unlike
271 their H2 inputs. Conversely, H2rn cells responded to contralateral regressive motion, as
272 excepted from their inputs from H2 cells, but they also responded to progressive motion (**Fig.**
273 **3-S2c**) despite not receiving direct input from HS cells. Thus, additional inputs from the central
274 brain likely convey visual information indirectly to H2rn cells. Nevertheless, responses to
275 binocular asymmetric stimuli were larger than monocular stimuli in all cells (**Fig. 3d-e**),
276 suggesting binocular interactions at the intermediate layer. Together, these findings
277 demonstrate that the sensitivity to optic flow in different classes of interneurons within the H2-
278 HS network are modulated by network activity and their central inputs, with strong binocular
279 interactions. Specifically, both uLPTCrns and bIPS display binocular optic flow selectivity that
280 cannot be entirely explained by their direct H2 inputs.

281 **Neurons within the H2-HS network show distinctive optic flow selectivity**

282 The lack of responses to contralateral regressive motion in bIPS and uLPTCrn
283 suggests that these interneurons might be equally sensitive to translational and rotational
284 optic flow. To test this idea, we examined their responses to binocular symmetric and
285 asymmetric stimuli (**Fig. 3-S2d**). We presented binocular translational motion or binocular
286 symmetrical horizontal motion (translation-like stimulus). The former stimuli contain
287 progressive or regressive horizontal components combined with vertical downward or upward
288 components, respectively, to mimic the visual consequence of the body's forward or backward
289 translation. The latter stimuli contain only horizontal progressive or regressive components,
290 representing what a horizontal-selective system may respond to in the context of translation
291 (**Supplementary Video 1,** "Progressive/regressive" and "Front-to-back/Back-to-front",
292 respectively). The three interneurons exhibited characteristic response profiles to these stimuli
293 (**Fig. 3d,e Fig. 3-S2d**). bIPS was most active with binocular symmetric horizontal stimuli
294 compared to translational progressive stimuli (**Fig. 3d,e**). uLPTCrn cells showed minimal or
295 negative responses to translational patterns, while H2rns showed positive response to both
296 regardless of the direction of motion, albeit weakly (**Fig. 3d,e, 3-S2d**).

297 To describe the relative selectivity of HS, H2, bIPS, uLPTCrns, and H2rns to rotational
298 vs. translational stimuli by calculating the discrimination index (see **Methods**, **Fig. 1-S1e**, **3f**).
299 HS and H2 responded to both rotational and translational optic flow. However, they were
300 relatively, albeit weakly, more selective to rotational optic flow, resulting in a slightly negative
301 discrimination index closer to zero compared to uLPTCrn and H2rn cells, which showed
302 enhanced selectivity for rotational optic flow, particularly when compared to the more
303 naturalistic translational optic flow. bIPS also responded to both rotational and translational
304 patterns in a selective manner; however, bIPS exhibited a relatively stronger sensitivity to
305 binocular horizontal symmetric stimuli and thus have a discrimination index skewed more
306 towards translations compared to rest of the H2-HS network cells (**Fig. 3f**).

307 We expanded our translational optic flow characterization (**Fig. 3-S3a**,
308 **Supplementary Video 1**) and observed that bIPS, like HS and H2 cells, exhibited its strongest
309 translational sensitivity to compound optic flow-fields, with sideslip and forward components
310 (**Fig. 3-S3b-d**). However, translational patterns with backwards motion which elicited activity
311 in H2 cells (**Fig. 3-S3c**) have minimal impact on bIPS. H2rns and uLPTCrns on the other hand,
312 minimally increased or decreased their activity during forward and backward translations (**Fig.
313 3-S3e-f**), becoming mostly sensitive to changes in sideslip translations (**Fig. 3-S3g**). Taken
314 together, these results demonstrate that neurons downstream of HS and H2 cells have
315 increased selectivities to characteristic patterns of optic flow. The question remains as to how
316 a neuron like bIPS, which is embedded in a rotational-sensitive network, enhances its
317 selectivity for translational or translational-like optic flow patterns, and what function this
318 response property provides to the network.

319 **Inhibitory interactions fine tune optic flow sensitivity in bIPS**

320 We hypothesized that the lack of responses to contralateral regressive motion in bIPS,
321 and its enhanced selectivity to translational optic flow could arise from recurrent interactions
322 between excitatory LPTCs and inhibitory interneurons. For example, excitation provided by
323 H2 to bIPS could be suppressed by indirect, H2-dependent inhibition. To identify possible
324 candidates, we analyzed the predicted neurotransmitter[52] for bIPS input neurons (**Fig. 4a**).
325 The two main inputs to bIPS are uLPTCrn and H2rn, both of which are GABAergic (**Fig. 4-S1**)
326 and receive prominent inputs from H2 (**Fig. 4b**). The subcellular organization of H2, HS,
327 uLPTCrn and H2rn inputs relative to the root point of bIPS (**Fig. 4-S2a**) suggests that these
328 neurons tend to make synapses closer to the root point than other bIPS inputs (**Fig. 4-S2b-
329 c**). H2rn synaptic inputs onto bIPS tend to be closer to H2 inputs than HS inputs (**Fig. 4-S2d**),
330 often forming microcircuit motifs with H2 (**Fig. 4-S2e, g**) but not with HS cells (**Fig. 4-S2f, h**).
331 Thus, this local connectivity structure could suppress H2-related excitation through H2rns, but

332 it may not fully account for the lack of responses to contralateral regressive motion in bIPS
333 (**Fig. 3-S2c**). Another possibility is that both H2rns and uLPTCrns contribute to this
334 suppression.

335 To test this idea, we perturbed fast-acting GABA signaling in bIPS using the FlpStop
336 genetic strategy[53]. We targeted the Resistance to dieldrin (Rdl) gene[54] since it is essential for
337 functional $GABA_A$ receptors[55,56] (GABAARs). Overall, bIPS' responses to optic flow Rdl-
338 FlpStop flies were decreased relative to control flies (**Fig. 4c-e**), including lack of negative
339 calcium responses to non-preferred directions of stimulus motion (**Fig. 4c-d**). Notably, the
340 effect of disrupting $GABA_A$ signaling was most evident for translational and translational-like
341 optic flow (**Fig. 4c-e**). This caused the discrimination index between translational-like and
342 rotational optic flow responses to skew towards zero (i.e., equal discriminability), while the
343 discrimination index between translation and rotational optic flow remained unaffected (**Fig.
344 4f**). These results suggest that the enhanced selectivity to horizontal binocular symmetric
345 motion, as well as the responses to the non-preferred directions of motion are mediated by
346 GABAARs in bIPS. However, contralateral regressive responses that drive H2 activity remain
347 unaffected under Rdl-FlpStop (**Fig. 4c**, "left CW"), indicating that signals from H2 are gated
348 by other mechanisms. Taken together, these findings show that GABAergic inhibition
349 modulates bIPS' selectivity to binocular symmetric optic flow within the network. We propose
350 that this selectivity may play a key role in enhancing the asymmetries in the activity of left
351 versus right postsynaptic partners, particularly in the sensory context of translational optic flow
352 where the visual input becomes more symmetric (**Fig. 1**).

353 **Reciprocal inhibitory connections in the middle layer of the H2-HS network promote
354 competition between the left and right sides for steering control**

355 Our Rdl-FlpStop experiments suggest that inhibitory input onto bIPS enhances its
356 responses to binocular symmetric stimuli. Because bIPS is an inhibitory neuron, its selectivity

357 may facilitate the detection of minor binocular asymmetries at the output layer of the network.
358 However, bIPS is embedded in a reciprocal motif with contralateral uLPTCrns (**Fig. 3a**),
359 making it challenging to understand the role of this motif in a dynamic setting like locomotion.
360 Therefore we implemented a phenomenological model agent[33] constrained by the connectivity
361 structure of the HS-H2 network (**Fig. 5, 5-S1**, see **Methods**), to study the role of bIPS and
362 uLPTCrns on steering control. Our agent processes horizontal motion to guide steering of a
363 virtual fly, like an exploratory real fly[39]. We built a model with four input channels, each
364 containing classical visual motion detectors[28], and the core cross-inhibitory circuit architecture
365 of the H2-HS network (**Fig. 5a**). The model was tuned to match the real neural data for
366 horizontal motion stimuli (see **Methods**, **Fig. 5-S1a-c** and **5b**).

367 We tested the effect of removing the inhibitory input to bIPS in the model by removing
368 ipsilateral uLPTCrns inputs. This manipulation abolished the enhanced responses of bIPS to
369 binocular symmetric stimuli (**Fig. 5c**) and affected the discriminability of the modeled cell to
370 rotational vs translational-like stimuli, like in the real fly (**Fig. 5d**). Based on these results, we
371 concluded that this simplified core model architecture, combining direct excitation with lateral
372 disinhibition, can replicate the visual responses of the input and middle layers of the H2-HS
373 subnetwork.

374 Next, we tested the contribution of the lateral inhibition provided by bIPS to the output
375 responses of the network in the context of course control. This agent fly compares the activity
376 of a left and right pair of DNs, akin DNp15, to impose steering control (**Fig. 5e**). Removing
377 bIPS from the model reduced the asymmetry between left and right DNp15 cells, leading to a
378 reduced ability to discriminate asymmetries in binocular horizontal motion during translations
379 at high speed (**Fig. 5f**). Removing both uLPTCrns and bIPS further reduced the asymmetry
380 between left and right DNp15 activity down to the level of HS. Like DNp15, activity of uLPTCrn
381 cells across the two eyes also became more symmetric upon removing bIPS (**Fig. 5f**).
382 Conversely, removing uLPTCrn cells made bIPS less sensitive to horizontal symmetric

383 binocular motion (**Fig. 5c**). Thus, the reciprocal inhibitory and lateral interactions within the
384 middle layer of the H2-HS network support enhanced sensitivity to differences between the
385 eyes at the output layer in the context of translations. Indeed, the asymmetry in DNp15 and
386 uLPTCrn cells remained high in ranges of forward velocities typically observed in exploratory
387 flies, and we propose that this is aided by the increased symmetric activity in bIPS as a
388 function of translation speed (**Fig. 5g**).

389 To test the direct contribution of bIPS to steering in the context of highspeed
390 translation, we allowed our agent fly to freely explore a virtual arena where the fly's trajectory
391 was determined by bouts of straight walking (forward runs) and rapid turns (saccades) away
392 from the walls, similar to real flies exploring a comparable environment (**Fig. 6a, 5-S1d,** see
393 **Methods**). As expected by model design, 'silencing' individual DNp15 cells predicted the
394 angular bias observed in real flies under individual DNp15 silencing (**Fig. 6b,** see also **Fig.**
395 **1i**). Silencing individual bIPS neurons in the model induced biases during forward runs and
396 performing the similar perturbation in real flies lead to similar results (**Fig. 6c, 6-S1a**). This
397 finding demonstrated that asymmetries between left and right bIPS activity, consistent with
398 the neuron's translational optic flow selectivity (**Fig. 3-S3**), are sufficient to bias the course
399 direction of walking flies (**Fig. 6c**). Consistent with the model, bilateral manipulations of activity
400 of bIPS did not affect the course of forward runs of real flies (**Fig. 6d**).

401 In summary, our findings support the idea of a central multilayer network that monitors
402 rotational components of optic flow during translation and that amplifies asymmetric activity
403 between right- vs. left outputs by lateral, competitive disinhibition, thereby increasing the
404 rotational signal even in the context of prominent translational optic flow (**Fig. 6e**). This
405 reciprocal, lateral inhibition therefore supports robust optic flow processing and increases the
406 performance of networks contributing to course control, two functions that are especially
407 important while walking at high speed.

408 ## Discussion

409 In this study we investigated how visuomotor circuits discriminate sensory signals in
410 challenging circumstances imposed by an animal's own locomotion. Through a combination
411 of full-brain EM reconstruction, modeling, optical imaging and behavior experiments, we
412 discovered a multi-layer network in the *Drosophila* central brain responsible for robust optic
413 flow processing and steering of exploring flies based. The first layer consists of optic flow
414 sensitive visual projection neurons, which form two networks with distinct sets of interneurons
415 and outputs. Both networks exhibit specific and recurrent connections between LPTCs and a
416 set of GABAergic inhibitory interneurons. Furthermore, there are critical reciprocal and lateral
417 interactions among the middle layer and across the hemispheres. The output layers receive
418 direct and indirect connections from the input layer, with the indirect pathway strongly
419 influenced by lateral disinhibition of the middle layer. This configuration allows the output
420 layer to generate a robust estimate of the fly's rotations, as indicated by their visual
421 consequence. Our findings unveils a network motif of competitive disinhibition[4] that enhances
422 the detection of asymmetries in optic flow across the eyes, enabling course control even in
423 the presence of highly symmetric bilateral visual motion cues (**Fig. 6e**).

424 **Parallel networks process visual feedback in the fly brain**

425 Until now, the few identified neck motor and descending outputs of HS and VS cells
426 have been shown to connect to either HS or VS cells[30,37,57,58] (CNMN6[59] being the single
427 exception). As such, HS and VS cells have been proposed to contribute to movement control
428 through largely parallel pathways. However, if downstream circuits of these LPTCs do not
429 converge, how can flies accurately estimate their self-movement when their natural
430 maneuvers during locomotion involve multiple axes of rotation and translation? By identifying
431 the major synaptic partners of HS, H2 and VS cells in the central brain (**Fig. 2**) we have found
432 that these LPTCs operate largely in parallel, connecting to distinct sets of descending, neck

433 motor and central brain output neurons. However, HS, H2 and VS cells also converge onto
434 anatomically distinct classes of GABAergic interneurons in the posterior slope. These
435 interneurons recurrently connect to different and complementary combinations of HS, H2 and
436 VS, suggesting the integration of orthogonal axes of optic flow at the central brain (**Fig. 3**).
437 We propose that this partially overlapping recurrent motif enables accurate processing of
438 naturalistic optic flow, modulating the concerted activity of LPTCs based on distinct visuomotor
439 conditions, and other internal contexts. Indeed, the identified inhibitory classes receive inputs
440 from motor and premotor areas of the fly CNS, including the VNC, PS, and GNG (**Fig. 2-S3**).
441 This feedback structure indicates strong processing of multimodal signals to differentially
442 modulate the activity of LPTCs and their postsynaptic outputs. These outputs likely contribute
443 to different motor programs and higher-order functions. For example, outputs of the H2-HS
444 network such as DNa02[47], DNp15[30,37] and VCNMN[57,60,61] have all been proposed to control
445 rotations of the body and the head along the yaw axis, while outputs of the VS subnetwork
446 such as DNp20 and ocelli have been implicated in gaze stabilization control along the roll
447 axis[60,62,63]. Each network project to neck-, leg-, and haltere-related regions in the VNC,
448 implicating LPTCs in the control of head and body movement independently but likely within
449 the context of head-body coordinated (gaze) motor programs occurring during exploratory
450 walking[39,64] and flight[65]. Additionally, output pathways that bridge LPTC activity with higher-
451 order brain regions, such as lateral accessory lobe and central complex via PS047, can
452 provide accurate internal self-motion estimates for heading perception and path integration
453 during navigation[66–69].

454 **GABAergic inhibition modulates asymmetries in visual motion processing**

455 Three cell types in the intermediate layers of H2-HS subnetwork, namely bIPS,
456 uLPTCrn and H2rn cells, exhibit optic flow sensitivities that are only partially explained by their
457 upstream LPTCs. This finding indicates that additional inputs influence their optic flow

458 sensitivity (**Fig. 3**). We have identified one group of such inputs: reciprocal connections among
459 the three cell types. These connections play a critical role in transforming optic flow signals
460 within the middle layer. For example, when fast acting GABAergic inputs to bIPS are
461 disrupted, the negative response caused by non-preferred directions of optic flow is eliminated
462 (**Fig. 4**). This effect is similar to the modulation of non-preferred visual motion responses in
463 the fly early visual system[70,71]. Furthermore, the same perturbation reduces bIPS' selectivity
464 to symmetric horizontal optic flow. Our constrained model suggests that this reduction is
465 partially caused by the inhibitory population of uLPTCrns, thereby likely affecting the
466 enhanced sensitivity to rotational optic flow by the output of the network. However, and
467 contrary to the expectations based by the connectivity structure, rapid GABAergic inputs do
468 not influence bIPS's responses to regressive, back-to-front optic flow. Although bIPS receive
469 strong connections from H2, signals from these synapses are not transmitted under non-
470 behaving conditions. One possibility is that the GABAergic population of H2rns controls this
471 signaling through other GABA receptors in bIPS. Alternatively, the gating of regressive signals
472 from H2 may involve other mechanisms, including neuromodulation. Further investigation will
473 explore the conditions under which bIPS respond to regressive information, which may render
474 the neuron more sensitive to asymmetric optic flow stimuli. Nevertheless, this finding
475 highlights the importance of combining EM connectivity with physiology to uncover context-
476 dependent modulation of brain circuits.

477 **Reciprocal inhibition in optic flow networks supports corrective steering**

478 A straightforward circuit for angular course control based on optic flow can be created
479 by connecting two rotational optic flow detectors (e.g., HS cells) separately to two rotational
480 actuators (e.g., DNp15). Such a system performs well when there is a significant difference in
481 activity levels between the two sensors. However, it performs poorly in detecting rotations
482 when the animal is moving forward at high speeds, which is surprisingly the condition where

483 HS cells contribute the most to corrective steering[35,36]. Furthermore, locomotion requires
484 continuous adjustments due to internal sources of noise, such as muscular and sensorimotor
485 noise, as well as uncertainties in the environment. These adjustments cause the optic flow to
486 be non-stationary, even when the fly intends to maintain a fixed course[72].

487 We propose two critical roles for the inhibitory motifs identified in the H2-HS network.
488 Firstly, it allows comparing the activity state of LPTCs across the two hemispheres and
489 provides cross-inhibition to silence competing inhibitory neurons, leading to a binary choice of
490 turning left or right. Similar circuit motifs with cross-inhibitory neurons in the hindbrain of
491 Zebrafish[73] and the vertebrate superior colliculus[74] bias angular movements in opposite
492 directions when activated or inhibited asymmetrically. Our experiments with bIPS yield
493 analogous results (**Fig. 6c**). Secondly, the inhibitory motifs can adjust the gain of LPTCs
494 during highspeed locomotion, allowing them to flexibly respond to changes in external and
495 internal conditions. Notably, bIPS provides prominent contralateral inputs to inhibitory
496 feedback CH cells, which project from the posterior slope back the lobula plate. CH cells
497 receive more than 450 synapses from bIPS (**Fig. 2-S1**). It is possible that bIPS corresponds
498 to the previously hypothesized *Horizontal unknown* cell, which provides binocular information
499 to CH cells through contralateral inhibition[75], thus playing a major role in integrating horizontal
500 motion from both eyes. Given its selectivity and inputs from motor and premotor regions, bIPS
501 is well suited for monitoring the fly's motor state, modulating descending neurons, feedback
502 pathways, and central pathways during periods of straightforward walking. This class of cells
503 also instructs optic flow processing, self-motion estimation and steering in the presence of
504 angular drifts. Therefore, bIPS contributes to the modulation of optic flow processing in a
505 multilayer manner.

506 **Estimation of self-motion from the eyes down to premotor and motor centers**

507 Optic flow-sensitive neurons have long been proposed to be integral components of
508 vital visuomotor circuits that enable animals to accurately perceive heading and control their
509 gaze and steering. In flies, while we have made substantial progress in understanding how
510 light reaching the photoreceptors are processed to detect visual motion and stimulate HS, H2,
511 VS cells and other LPTCs[28,76], our knowledge of how downstream pathways are organized
512 and process optic flow has remained far more limited. With the comprehensive description of
513 the HS, H2 and VS networks outlined here, and the visual and behavioral analysis of neurons
514 within these networks, we now possess a framework to establish mechanistic links between
515 visual activity in these networks and the ongoing locomotion control of a freely moving fly.
516 Given the common characteristics of optic flow and associated visual neurons processing
517 across different animal species[77,78] and the universal constrains on locomotive systems, the
518 findings reported here have the potential to shed light on how analogous systems in other
519 animals are functionally organized to process naturalistic optic flow in support of navigation.

520 Acknowledgements

521 We thank Ruchi Parekh and Janelia CAT for introducing us to FAFB and training us in EM
522 tracing. Kaylynn Coates and Feng Li for reviewing some of our manually traced neurons in
523 FAFB. Stephen Huston for early tracing of VCNMN and some cLPTCrn cells with Shahrozia
524 Imtiaz and for helping identify neck motor neurons. Anna Li and Rachel Wilson for their help
525 in reconstructing DNa02. Shigehiro Namiki and Gwyneth Card for their help in identifying
526 descending neurons. Jens Goldammer for identifying potential split-Gal4 candidates for H2rn
527 cells and helping identify S-Neurons. Hideo Otsuna, Greg Jefferis and Phillip Schlegel for
528 introducing us to their tools for computational neuroanatomy and for helping with EM data
529 analysis. Arthur Zhao for his input on LPTC naming, response predictions, and feedback on
530 the manuscript. Nils Eckstein and Jan Funke for sharing neurotransmitter predictions for LPTC
531 partners prior to publication. Gaby Maimon and Cheng Lyu for sharing sytGCaMP7f flies prior

to publication. Marion Silies for sharing the UAS-GCaMP6f, UAS-FLP recombinant line. Ece Sönmez for help with testing Split-Gal4 combinations and help with validating FlpStop recombinants. CR Fly Platform for assisting fly stock generation, maintenance, and GABA stainings. Lalanti Venkatasubramanian for her help with the initial bIPS>TrpA1 behavior experiments. Terufumi Fujiwara for help with finding and testing potential Split-Gal4 combinations for H2rn and uLPTCrn and help with building the 2-photon calcium imaging set up. André Marques and Wynne Stagnaro for sharing unpublished work about multisensory processing in LPTCrn and bIPS cells. Past and present Chiappe Lab members for useful discussions and feedback on experiments and the manuscript. This work was supported by the Champalimaud Foundation and the research infrastructure Congento, LISBOA-01-0145-FEDER-022170. MECh is supported by European Research Council Starting Grant ERC-2017-STG-759782 537.

Author Contributions

In alphabetical order:

Davi D Bock: Generation of FAFB dataset and allowing access pre-publication. Resources & Data Curation.

Margarida Brotas: Reconstruction and review of 1st and 2nd order LPTC partners and cross-matching LPTC partners across EM datasets. Investigating differences in anatomy, connectivity, and neurotransmitter profile among LPTC partners.

M Eugenia Chiappe: Conceptualization. Methodology. Supervision. Resources. Funding acquisition. Writing – original draft. Writing – Review & Editing. Visualization.

Tomás Cruz: Design, running and analysis of DNp15>hsFLP,Kir experiments. Provide input, feedback and initial scripts to parse and analyze behavior data. Behavioral agent simulations with the modeled network.

556 **Mert Erginkaya**: Conceptualization. Reconstruction and review of LPTC synaptic
557 partners and some LPTCs in FAFB. Reconstruction and review of 2nd order
558 inputs/outputs of LPTC networks. Cross-matching LPTC partners across EM
559 datasets. Analysis of EM anatomy & connectivity. Generation of all transgenic lines.
560 GABA stainings (with the help of Fly Platform). Designing, performing, and analyzing
561 calcium imaging experiments. Design and analysis of behavior experiments.
562 Visualization of data and writing the paper.

563 **Aljoscha Nern**: Generation of transgenic lines that label LPTCrns. Re-injection of
564 uLPTCrn Gal4 line. Input for split candidates for bIPS. EM-LM cell identification and
565 naming for several cell types.

566 **Michael B Reiser**: Conceptualization. Reconstruction of LPTCs in FAFB and
567 proofreading LPTCs in FlyWire and Hemibrain (by Reiser Lab tracers). Naming
568 LPTCs. Help with generating optic flow stimulus patterns in LED arena (Software, from
569 Matthew Isaacson). Regular feedback on EM tracing status & priorities, and feedback
570 on calcium imaging experiments.

571 **Kathrin Steck**: Reconstruction and review of LPTC partners in FAFB. Reconstruction
572 and review of 2nd order inputs/outputs of LPTC networks.

573 **Filipa Torrão**: Investigating differences in connectivity among LPTC partners.
574 Analysis of local connectivity structure within bIPS dendrites (**Fig. 6-S2**)

575 **Nélia Varela**: Generation of transgenic lines that label bIPS, H2rn, H2, HS.
576 Immunostainings and images for several transgenic lines. Performing behavioral
577 experiments. Immunostainings for individual bIPS>hsFLP,Kir and DNp15>hsFLP,Kir
578 and MCFO flies.

Inclusion and Diversity Statement

While citing references scientifically relevant for this study, we worked to promote gender balance in our reference list as much as possible

Declaration of Interests

The authors declare no competing interests

Tables

Supplementary Table 1: Cross-matching of LPTC outputs across EM dataset

H2 Output Cells	FlyWire rank	FAFB rank	Hemibrain rank
PS047	3	1	3
VCH	1	2	2
DCH	2	3	1
DNp15	4*	4	4
bIPS	5	5	5
CNMNx	34*	6	11**
DNb03	6	7	7
DNb03	8	8	8
DNg41	9	9	6**
uLPTCrn	11	10	9
PS126	10	12	28
PS099	7	31	48
PS081	14	16	10
HS Output Cells	**FlyWire rank**	**FAFB rank**	**Hemibrain rank**
bIPS	1	1	2
DNp15	2*	2	1
PS047	4	3	3
CNMNx	21*	4	4**
VCNMN	5	5	7**
DNa02	3	6	9
uLPTCrn	10	7	5
lVLPT8	8	8	35
uLPTCrn	16	9	6
uLPTCrn	13	10	10
PLP195	6	11	29
DNgX	7	26	

DNa04			8
VS Output Cells	**FlyWire rank**	**FAFB rank**	**Hemibrain rank**
DNp20	1*	1	2
DNb06	2	2	
cLPTCrn	4	3	10
CNMN6	6	4	6
CNMN7	31	5	
cLPTCrn	7	6	20
uLPTCrn	40	7	5
PS126	3	8	7
S-Neuron	45	9	8
S-Neuron	38	10	9
DNge043	5	48	3
DNp22	8	70	
PS135	9	37	1
cLPTCrn	10	12	16
PS169	48		4

586

587 * FlyWire segmentation or synapse predictions are of low quality

588 ** Uncertain hemibrain matching, since it is based on a small neural arbor cut off at the limits

589 of the dataset

590 **Supplementary Table 2: List of neurons within the LPTC central brain network**

#	FAFB ID	FlyWire segment ID*	FlyWire soma coordinates	Hemibrain ID	Hemibrain cell type
1	Right uLPTCrn 2918805 PG ME	720575940628599516	114786, 73911, 1623		PS070-PS074
2	Right uLPTCrn 11965240 ME	720575940631296543	113632, 74374, 1687		PS070-PS074
3	Right DNg41 15463855 MB	720575940617611643	99290, 75988, 3794	5813024629**	
4	Right uLPTCrn 2549438 ME	720575940631333955	109930, 75338, 1666		PS070-PS074
5	Right uLPTCrn 2544668 ME	720575940612144047	112472, 73317, 1957		PS070-PS074

6	GNG neuron 2948699 ME	720575940648969337	121455, 91088, 2979		
7	DCH neuron (right) 1077175 ZSG-GA	720575940640039989	131955.27, 53517.50, 1223.00	1466485353	DCH
8	VCH neuron (right) 1078536 GA-ZSG	720575940627138562	134785, 53191, 958	5813024201	VCH
9	Putative CNMN 5218081 ME	720575940622008560***	105319, 78004, 4717	2180780757**	
10	VCN002 DB	720575940635776760***	124703, 91385, 3579	2428058771**	
11	DNa02_AL	720575940629327659	101150, 42526, 2117	1140245595	DNa02
12	neuron 7828867 BG	720575940621564329	104740, 50998, 5510		PLP195
13	DNgX 999559 ME	720575940614730914	105915, 76095, 4569	1874217622**	
14	Putative Right cLPTCrn 410927 SI	720575940642061709	112863, 73654, 2042		PS079
15	Right cLPTCrn 410809 SI	720575940617997396	113277, 73467, 2192		PS079
16	Right bLPTCrn 416268 ME	720575940608760110	112920, 74883, 1730		PS078
17	Right bLPTCrn 986687 ME	720575940620555696	111749, 73943, 2041		PS078
18	Right uLPTCrn 2500746 ME	720575940606873522	112559, 74568, 1653		PS070-PS074
19	Right uLPTCrn 1002426 ME	720575940647708537	114241, 73636, 1682		PS070-PS074
20	Right DNp15 5224930 ME	720575940610301413***	120043, 60033, 5393	5813078134**	DNp15
21	Right bIPS neuron 3029744 ME	720575940622581173	125645, 88652, 4814	1932497911	
22	Right PS047 16769498 ME	720575940638306163	98755, 67802, 2032	1621806893	PS047

23	Left bIPS neuron 969206 ME	720575940623618708	141214, 90010, 4743	1963869636	
24	H2 neuron (left) 5232903 ME	720575940632427603	164810, 54592, 5192	5813078454	H2
25	Right DNb03 8416446530 ME	720575940620776880	105915, 58345, 1981		DNb03
26	Right H2rn 11956981 ME	720575940621865991	127153, 91186, 3928		
27	Right DNb03 413171 MB	720575940634163682	107706, 58941, 2096		
28	Right H2rn 11930922 ME	720575940622082451	128029, 91037, 3888		
29	Right H2rn 9730354 ME	720575940624756836	126229, 90972, 3889		
30	Right H2rn 8438890 ME	720575940617566769	127758, 91886, 3927		
31	Right H2rn 8178074 ME	720575940642076576	127930, 91367, 4018		
32	Putative VSN 851433 ZSG	720575940624931564	89397, 61348, 6667	5813033533	VS
33	Putative VSN 804093 ZSG	720575940633923298	82426, 57153, 6848	1558230909	VS
34	neuron 5207415 ME	720575940613940074	83118, 55640, 4101	1221457679	IVLPT8
35	Putative HSN 830794 ZSG	720575940628031249	91612, 60674, 6567	2211443902	HSN
36	Putative HSE 827035 ECS ZSG	720575940642723981	98857, 55902, 5783	1807537598	HSE
37	Putative HSS 408972 SJH ZSG	720575940622312965	94341, 61845, 6407	2179731270	HSS
38	VSN-Like 982898 ZSG	720575940626477498	86531, 61966, 6790	5813024262	VS
39	putative VSN 793033 ZSG	720575940615269794	82514, 59151, 6836	1868619183	VS
40	Putative VSN 815777 ZSG	720575940622831740	84905, 55521, 6704	5813025091	VS

41	Putative VSN 852994 JLME ZSG	720575940633017939	82465, 56046, 6799	1557885051	VS
42	Putative VSN 807402 ZSG	720575940626457406	85387, 60389, 6811	1868255513	VS
43	putative VSN 804540 ZSG	720575940605688492	84584, 57582, 6777	1992161820	VS
44	Right S-Neuron 4906099 ME	720575940629666971	126241, 28340, 3824		OCG07
45	Right S-Neuron 4905400 ME	720575940625314547	127007, 30053, 4080		OCG07
46	Right S-Neuron 4880581 ME	720575940609826499	127788, 30884, 4072		OCG07
47	Right DNOVS1 9937342 ME	720575940629390123***	115510, 45447, 4960	1745333830**	DNp20
48	Right DNb06 9857697 ME	720575940637308605	126678, 68176, 1317	1715999506	DNb06
49	Right PS126 4905394 ME	720575940629701484	131516, 30646, 3039	1591156798	PS126
50	Left bLPTCrn 9157628 ME	720575940631876577	149420, 77362, 1632		PS078
51	Right bLPTCrn 17646150 ME	720575940624461543	113818, 75477, 1710		PS078
52	Right bLPTCrn 869476 ME	720575940628284931	113237, 74767, 1898		PS078
53	Putative Right bLPTCrn 1934541 ME	720575940605344434	113968, 76236, 1733		PS078
54	Cervical Nerve Neuron 1337778 SI	720575940633404627	118851, 65265, 5421		
55	Cervical Nerve Neuron 1167859 SI	720575940621583286	119957, 62874, 5368		
56	Left bLPTCrn 9369685 ME	720575940610505881	148617, 76818, 1461		PS078

57	Right cLPTCrn 968975 ME	720575940625557069	110736, 74923, 2028		PS079
58	Left cLPTCrn 414149 ME	720575940607991819	146347, 76067, 1244		PS079
59	Left cLPTCrn 2725485 ME	720575940629929273	147252, 76791, 1398		PS079
60	Left cLPTCrn 1006244 SI	720575940612306641	146666, 75707, 1607		PS079
61	Right cLPTCrn 414194 ME	720575940620867254	112846, 70948, 2282		PS079
62	Right cLPTCrn 1051520 SI	720575940629267531	111884, 74761, 2203		PS079
63	Left cLPTCrn 967831 ME	720575940624324708	147231, 75756, 1219		PS079
64	Putative Right cLPTCrn 9336219 ME	720575940631645009	111149, 73533, 1804		PS079
65	Left cLPTCrn 4881422 ME	720575940626420220	146247, 75467, 1279		PS079
66	Right cLPTCrn 969249 ME	720575940620263088	111942, 73451, 1739		PS079
67	Left cLPTCrn 952121 ME	720575940616362123	148068, 76482, 1602		PS079
68	Left cLPTCrn 412520 ME	720575940621845119	147390, 76088, 1339		PS079
69	Right cLPTCrn 2560372 ME	720575940628688246	113125, 72872, 1901		PS079
70	Right cLPTCrn 411566 ME	720575940619872751	113686, 72642, 2212		PS079
71	Left cLPTCrn 1027141 SI	720575940635634680	145378, 76025, 1378		PS079
72	Right cLPTCrn 968122 ME	720575940621147425	114031, 73227, 1620		PS079

591 * As of 230422

592 ** Uncertain hemibrain matching, due to incomplete hemibrain skeleton

593 *** Bad or incomplete segmentation in FlyWire

594 **Supplementary Table 3: List of fly lines used in each figure**

Figure(s)	Panel(s)	Target cell type(s)	Genotype(s)
1	d, e	DNp15	w^{1118}; R11E07-p65.AD / 20XUAS-jGCaMP7f; R77F05-Gal4.DBD / 20xUAS-6XmCherry; 13XLexAop-jGCaMP7f; R77F05-LexA; +;
1	f, g	DNp15	hsFLP; R11E07-p65.AD / +; R77F05-Gal4.DBD / 10XUAS>Stop>eGFPKir2.1;
1-S1		DNp15	w^{1118}; R11E07-p65.AD / 20XUAS-jGCaMP7f; R77F05-Gal4.DBD / 20XUAS-6XmCherry; 13XLexAop-jGCaMP7f; R77F05-LexA; +;
1-S1	f, g	DNp15	hsFLP; R11E07-p65.AD / +; R77F05-Gal4.DBD / 10XUAS>Stop>eGFPKir2.1;
1,1-S1,3,3-S2,3-S3		HS	w^{1118}; R27B03-p65.AD / 20XUAS-6XmCherry; R39E01-Gal4.DBD / UAS-sytGCaMP7f; w^{1118}; 20XUAS-jGCaMP7f / +; VT058487-Gal4 / UAS-CD4::tdTomato w^{1118}; R39E01-LexA, 13XLexAop2-6XmCherry / +; VT058487-Gal4 / UAS-sytGCaMP7f
3,3-S2,3-S3		H2	w^{1118}; R23C12-p65.AD / 20XUAS-6XmCherry; R32A11-Gal4.DBD / UAS-sytGCaMP7f; w^{1118}; R23C12-p65.AD / R39E01-LexA, 13XLexAop2-6XmCherry; R32A11-Gal4.DBD / UAS-sytGCaMP7f
3,3-S2,3-S3		bIPS	w^{1118}; R25F07-p65.AD / 20XUAS-6XmCherry; VT014724-Gal4.DBD / UAS-sytGCaMP7f; w^{1118}; R25F07-p65.AD / 20XUAS-jGCaMP7f; VT014724-Gal4.DBD / UAS-CD4::tdTomato
3,3-S2,3-S3		H2rn	w^{1118}; VT040346-p65.AD / 20XUAS-6XmCherry; VT049923-Gal4.DBD / UAS-sytGCaMP7f;
3,3-S2,3-S3		uLPTCrn	w^{1118}; 20XUAS-6XmCherry / +; R50G03-Gal4 / UAS-sytGCaMP7f; w^{1118}; R39E01-LexA, 13XLexAop-6XmCherry / +; R50G03-Gal4 / UAS-sytGCaMP7f
3-S1	a	bIPS	w^{1118}; R25F07-p65.AD / UAS-mCD8::GFP; VT014724-Gal4.DBD / +;
3-S1	a	H2rn	w^{1118}; VT040346-p65.AD / UAS-mCD8::GFP; VT049923-Gal4.DBD / +;

Figure(s)	Panel(s)	Target cell type(s)	Genotype(s)
3-S1	a	uLPTCrn	w^{1118}; Otd-nls:FLPo / +; R50G03-Gal4 / pJFRC56-10XUAS>Stop>eGFPKir2.1;
3-S1	a	LPTCrn	w^{1118}; VT045281-p65.AD / Otd-nls:FLPo; VT038829-Gal4.DBD / pJFRC56-10XUAS>Stop>eGFPKir2.1;
3-S1	a	HS	w^{1118}; R27B03-p65.AD / 20XUAS-jGCaMP7f; R39E01-Gal4.DBD / UAS-CD4::TdTomato;
3-S1	a	H2	w^{1118}; R23C12-p65.AD / UAS-2xEGFP; R32A11-Gal4.DBD / +;
3-S1	a	DNp15	w^{1118}; R11E07-p65.AD / 20XUAS-jGCaMP7f; R77F05-Gal4.DBD / 20XUAS-6XmCherry;
3-S1	b	LPTCrn	w^{1118} / MCFO-1; VT045281-p65.AD / +; VT038829-Gal4.DBD / MCFO-1;
3-S1	c	bIPS Rdl +/-	w^{1118}; R25F07-p65.AD / 20XUAS-GCaMP6f, UAS-FLP; VT014724-Gal4.DBD / $Rdl^{FlpStop\ ND}$;
3-S1	c	bIPS Rdl -/-	w^{1118}; R25F07-p65.AD / 20XUAS-GCaMP6f, UAS-FLP; VT014724-Gal4.DBD, $Rdl^{FlpStop\ ND}$ / $Rdl^{FlpStop\ ND}$;
4		bIPS Rdl +/+	w^{1118}; R25F07-p65.AD / 20XUAS-GCaMP6f, UAS-FLP; VT014724-Gal4.DBD / 20XUAS-6XmCherry;
4		bIPS Rdl -/-	w^{1118}; R25F07-p65.AD / 20XUAS-GCaMP6f, UAS-FLP; VT014724-Gal4.DBD, $Rdl^{FlpStop\ ND}$ / $Rdl^{FlpStop\ ND}$;
4-S1	a	LPTCrn	w^{1118}; VT045281-p65.AD / UAS-mCD8::GFP; VT038829-Gal4.DBD / +;
4-S1	a	uLPTCrn	w^{1118}; UAS-mCD8::GFP / + ; R50G03-Gal4 / +;
4-S1	a	bIPS	w^{1118}; VT014724-p65.AD / UAS-mCD8::GFP; VT039047-Gal4.DBD / +;
4-S1	a	H2rn	w^{1118}; VT040346-p65.AD / UAS-mCD8::GFP; VT049923-Gal4.DBD / +;
4-S1	b	LPTCrn ∩ GAD1	w^{1118}; UAS-mCD8::GFP / +; VT045281-Gal4.DBD / GAD1-p65.AD;
4-S1	b	LPTCrn ∩ ChaT	w^{1118}; VT045281-p65.AD / UAS-mCD8::GFP; ChaT-Gal4.DBD / +;
4-S1	b	LPTCrn ∩ VGlut	w^{1118}; VT045281-p65.AD / VGlut-Gal4.DBD; 40xUAS-mCD8::GFP;
4-S1	b	uLPTCrn ∩ GAD1	w^{1118}; UAS-mCD8::GFP / +; GAD1-p65.AD / R50G03-Gal4.DBD;
4-S1	b	uLPTCrn ∩ ChaT	w^{1118}; R50G03-p65.AD / UAS-mCD8::GFP; ChaT-Gal4.DBD / +;
4-S1	b	uLPTCrn ∩ VGlut	w^{1118}; R50G03-p65.AD / VGlut-Gal4.DBD; 40xUAS-mCD8::GFP;
4-S1	b	bIPS ∩ GAD1	w^{1118}; UAS-mCD8::GFP / +; GAD1-p65.AD / VT014724-Gal4.DBD;
4-S1	b	bIPS ∩ ChaT	w^{1118}; VT014724-p65.AD / UAS-mCD8::GFP; ChaT-Gal4.DBD / +;
4-S1	b	bIPS ∩ VGlut	w^{1118}; VGlut-p65.AD / UAS-mCD8::GFP; VT019845-Gal4.DBD / +;

Figure(s)	Panel(s)	Target cell type(s)	Genotype(s)
4-S1	b	H2rn ∩ GAD1	w^{1118}; UAS-mCD8::GFP / CyO; GAD1-p65.AD / VT049923-Gal4.DBD;
4-S1	b	H2rn ∩ ChaT	w^{1118}; VT040346-p65.AD / UAS-mCD8::GFP; ChaT-Gal4.DBD / +;
4-S1	b	H2rn ∩ VGlut	w^{1118}; VGlut-p65.AD / UAS-mCD8::GFP; VT049923-Gal4.DBD / +;
6	b	DNp15	hsFLP; R11E07-p65.AD / +; R77F05-Gal4.DBD / 10XUAS>Stop>eGFPKir2.1;
6	c	bIPS	hsFLP; R25F07-p65.AD / +; VT014724-Gal4.DBD / 10XUAS>Stop>eGFPKir2.1;
6	d	empty control >TrpA1 (control 1)	w^{1118}; Empty-p65.AD / UAS-TrpA1(B).K; Empty-Gal4.DBD / +;
6	d	bIPS #1 >TrpA1	w^{1118}; R25F07-p65.AD / UAS-TrpA1(B).K; VT014724-Gal4.DBD / +;
6	d	bIPS #2 >TrpA1	w^{1118}; VT014724-p65.AD / UAS-TrpA1(B).K; VT039047-Gal4.DBD / +;
6	d	bIPS #3 >TrpA1	w^{1118}; VT039047-p65.AD / UAS-TrpA1(B).K; VT019845-Gal4.DBD / +;
6	d	empty control > Kir2.1 (control 2)	w^{1118}; Empty-p65.AD / Otd-nls:FLPo ; Empty-Gal4.DBD / pJFRC56-10XUAS>Stop>eGFPKir2.1;
6	d	bIPS #1 > Kir2.1	w^{1118}; R25F07-p65.AD / Otd-nls:FLPo; VT014724-Gal4.DBD / pJFRC56-10XUAS>Stop>eGFPKir2.1;
6-S1	a	bIPS #1	w^{1118}; R25F07-p65.AD / UAS-mCD8::GFP; VT014724-Gal4.DBD / +;
6-S1	a	bIPS #2	w^{1118}; VT014724-p65.AD / UAS-mCD8::GFP; VT039047-Gal4.DBD / +;
6-S1	a	bIPS #3	w^{1118}; VT039047-p65.AD / UAS-mCD8::GFP; VT019845-Gal4.DBD / +;
6-S1	b	bIPS	hsFLP; R25F07-p65.AD / +; VT014724-Gal4.DBD / pJFRC56-10XUAS>Stop>eGFPKir2.1;

Figure legends

Figure 1: DNp15 exhibit enhanced sensitivity to rotational optic flow compared to HS and plays a role in steering during high-speed translation (**a**) Simulated binocular optic flow of a fly walking at low (left) versus high (right) forward speed and rotating with the same angular velocity. Rectangles indicate the presence of regressive (blue) or progressive (magenta) motion detected by a horizontal motion-sensitive system. (**b**) EM-reconstructed

602 right HS (magenta) and postsynaptic right DNp15 (olive) cells. The chemical and electrical
603 synapses between the two cells allocated within the inferior posterior slope (IPS, cyan), a
604 premotor region. The dendrites of HS cells are located within the lobula plate (LOP). (**c**) Top,
605 schematic of the fly brain and the IPS, where optical imaging was performed. Bottom, 2-
606 photon calcium imaging setup and the visual LED display. (**d**) HS (magenta) and DNp15
607 (olive) calcium responses to horizontal binocular rotational or translational-like optic flow (top),
608 and to monocular stimuli (bottom). (e) Discrimination index (see **Methods**) between
609 translational-like and rotational stimuli in HS (magenta) and DNp15 (olive). Each circle
610 represents an individual ROI. Colored horizontal line and black vertical line represent the
611 mean and 95% CI. (HS: N=12 flies, n=16 ROIs, DNp15: N=6 flies n=7 ROIs, *P < 0.05; **P <
612 0.01 ***P < 0.001, Wilcoxon's rank-sum test). (**f**) The walking paths of forward runs of length
613 ≥ 4 body lengths, aligned at their origin, in flies with either both or none DNP15 silenced (left,
614 light gray traces), right DNp15 silenced (middle, gray traces), and left DNp15 silenced (right,
615 black traces). (**g**) Left, definition of path deviation, the difference in body orientation between
616 the end and the beginning of the walking path over traveled distance. Right, mean path
617 deviation from per fly in flies with none, single or both DNp15 silenced. The size of the circle
618 indicates the number of walking bouts per fly, with larger sizes representing larger number of
619 walking bouts. Number of flies per condition, none n=25; both n=31; left n=22; right n=22; *p
620 < 0.05 **p < 0.01 ***p < 0.001, Wilcoxon's rank-sum test with Bonferroni correction for multiple
621 comparisons.
622
623 **Figure 2. H2, HS and VS cells form two distinctive networks in the central brain.** (**a**)
624 Connectivity graph of the H2-HS (left) and VS (right) networks. Neurons are represented as
625 nodes (circles), with their synaptic connections indicated by arrows (predicted to be excitatory)
626 or tee-shaped edges (predicted to be inhibitory). Thickness of the arrows/tee-shaped edges
627 represents number of synapses, and color indicates the presynaptic neuron. For clarity,

628 connections with fewer than 10 synapses are not shown; connections with fewer than 50
629 synapses are shaded. Node diameters represent the total number of connections that each
630 node has within the network (including both inputs and outputs). Except for LPTCs, nodes are
631 placed within the brain regions (grey rectangles) where their axons reside. (**b**) The total
632 number of synaptic connections for each neuron within H2-HS network (Top), and VS network
633 (bottom). See Supplementary Table 2 for the complete list of neurons and nomenclature. (**c**)
634 Connectivity graph between each LPTC input cell type and individual HS, H2 and VS cells.
635 Edges indicate synaptic connection between cells, with thickness indicating number of
636 synapses and color indicating the presynaptic cell. LPTCs without input are transparent for
637 clarity.
638
639 **Figure 3: Binocular interactions define optic flow sensitivity within the H2-HS network.**
640 (**a**) Local connectivity between the input and middle layers of the H2-HS network. (**b**) Left,
641 schematic of the central nervous system (CNS) regions from which uLPTCrns, bIPS and
642 H2rns receive inputs. LOP, lobula plate; ME, medulla; GNG, gnathal ganglia; IPS, inferior
643 posterior slope; SPS, superior posterior slope. Right, proportion of inputs per CNS region
644 (color code) for each interneuron. (**c**) Single plane fluorescence image of an example
645 recording from bIPS axons during binocular CW (top) and CCW (bottom) horizontal motion.
646 We defined a single region of interest (ROI), which covers the entire axon is outlined in white.
647 The red signal corresponds to mCherry fluorescence, whereas the green signal corresponds
648 to sytGCaMP7f fluorescence. Scale bar, 10 μm. (**d**) Top: visual stimuli presented to the fly,
649 with direction of motion as indicated by arrows. Bottom: optic flow calcium responses (OFR)
650 of each neuron to rotational (stimuli 1, 2, 3) or translational (stimuli 4, 5) optic flow. OFR for
651 rotational stimuli is defined as CW (rightwards) minus CCW (leftwards) direction of visual
652 motion. For the translational stimuli, OFR is defined as progressive minus regressive direction
653 of visual motion. Each trace corresponds to the grand mean of the z-scored calcium response

654 across flies ± SEM (shade). Per fly, we obtained mean responses to 5-10 repetitions per
655 stimulus. Light-gray rectangles indicate the stimulation window. For this and the remaining
656 panels: HS: N=12 flies n=16 ROIs, H2: N =8 flies n=11 ROIs, bIPS: N=10 flies n=11 ROIs,
657 H2rn: N=5 flies n=8 ROIs, uLPTCrn: N=6 flies n=8 ROIs. (**e**) Normalized OFRs (relative to the
658 preferred stimulus per neuron). Error bars represent SEM of the grand mean across flies. (**f**)
659 Left, discrimination index between translation-like vs. rotational stimuli (see **Methods**). Each
660 circle represents an individual ROI. The horizontal line and black vertical line represent mean
661 and 95% CI. Right, discrimination index between translation vs. rotational stimuli. *: $p < 0.05$;
662 **$p < 0.01$; ***$p < 0.001$, Wilcoxon's rank-sum test with Bonferroni correction for multiple
663 comparisons.
664
665 **Figure 4: GABAergic inhibition fine-tunes optic flow responses in bIPS.** (**a**) Right bIPS
666 input profile, grouped by their predicted primary neurotransmitter. Neurons shown in b) are
667 highlighted with colored lines. (**b**) Schematic of the local connectivity of the input and middle
668 layers of the H2-HS network. Inhibitory connections are shown as tee shaped edges. Blocking
669 Rdl receptors in bIPS using FLPStop disrupts fast GABAergic signaling onto bIPS (black
670 crosses). (**c**) Neural responses of wild-type (dark green) and Rdl-disrupted (light green) bIPS
671 cells to binocular asymmetric (left, rotational) and symmetric (right, translational-like) optic
672 flow (OF). Each trace corresponds to the grand mean ± SEM (shaded area) of z-scored
673 calcium responses obtained across flies. For each fly, mean responses to 5-10 repetitions per
674 stimulus were obtained from a single ROI at the axon terminals. Stimuli with a star indicate
675 area under the curve (auc) responses that are statistically different from wild type bIPS
676 recordings. (**d**) Same as **c**), but for translational optic flow. (**e**) OF responses, the difference
677 between the preferred and nulled direction responses (auc) for horizontal and progressive
678 visual motion. (**f**) Left, discrimination index between translational-like and rotational optic flow
679 of recorded neurons in c) (see **Methods**). Each circle represents an individual ROI. Colored

horizontal line and black vertical line represents mean and 95% CI. Right, discrimination index between progressive and rotational optic flow. For all panels: bIPS: N=7 flies n=9 ROIs, bIPS Rdl-FLPStop: N=7 flies n=10 ROIs. *P < 0.05; **P < 0.01 ***P < 0.001, Wilcoxon's rank-sum test.

Figure 5: A lateral disinhibitory motif enhance asymmetries in neural activity across the right versus left hemisphere. (**a**) Schematic of the agent architecture: two sets of Reichardt detectors tuned to front-to-back (FtoB) or back-to-front (BtoF) motion detect the optic flow generated by a simulated walking fly (See **Methods**, **Fig. 5-S1**). The detected visual motion is processed by a network of nodes that mimic the core network motif of H2-HS network (**Fig. 3a**). The weights that connect the nodes are tuned based on a subset of measured visual responses (**Fig. 5-S1**). (**b**) Simulated and observed visual responses to monocular and binocular patterns of optic flow. Responses were matched to the maximal observed response. Observed responses are replotted from **Fig. 3-S2** and **Fig. 4c** (**c**) Visual response of modeled bIPS to symmetric or asymmetric binocular optic flow, and with or without a functional input from uLPTCrns. (**d**) Left: discrimination index of modeled and observed bIPS with or without a functional input from uLPTCrns. Right: observed bIPS' discrimination index with or without functional GABAergic input (replotted from **Fig. 4f**). (**e**) Definition of the Asymmetry Index (AI) and two example conditions with low and high AI values. (**f**) Asymmetry index of simulated neurons (colored) in the full model (Control), under bIPS silencing (Without B), under uLPTCrn silencing (Without U) and under both bIPS and uLPTCrn silencing (Without U+B). The dot size corresponds to the magnitude of the neural response. (**g**) Asymmetry index of simulated neurons (colored) in the full model varying the forward velocity of the agent. The shaded area corresponds to the range of velocities observed for forward runs in real exploratory flies (Cruz et al. 2021)[39].

706 **Figure 6: bIPS plays a role in steering control during high-speed walking**. (**a**) Example
707 walking paths of the agent (left) and the real fly (right) under prominent visual feedback. (**b**)
708 Simulated (left) and real fly (right) angular bias during forward runs (see **Methods**) with DNp15
709 activity perturbed bilateral or unilaterally. Transparent dots depict mean bias of individual flies,
710 black dots represent grand mean per genotype, weighted by the amount of walking bouts (dot
711 size). Error bars represent SEM. Number of flies per condition, none n=25; left n=22; right
712 n=22; both n=31. (**c**) Same as b), but for bIPS. Number of flies per condition, none n=65; left
713 n=26; right n=38; both n=13. For (**b**) and (**c**): *p < 0.05; **p < 0.01 ***p < 0.001, Wilcoxon's
714 rank-sum test with Bonferroni correction for multiple comparisons. (**d**) Left, simulated
715 straightness of the agent during forward runs (see **Methods**) with control (green), bilaterally
716 activated (dark green) or silenced (light green) bIPS cells. Right, straightness of control flies
717 (green), or flies with bilaterally activated (dark green) or silenced (light green) bIPS cells.
718 Number of flies per condition, empty control>TrpA1 n=25; bIPS#1>TrpA1 n=27;
719 bIPS#2>TrpA1 n=25; bIPS#3>Tr-pA1 n=29; empty control>Kir2.1 n=22; bIPS#1>Kir2.1 n=23.
720 (**e**) Summary of the findings. The middle layer of the H2-HS network supports steering by
721 enhancing the difference in the activity levels of the output layer across hemispheres. This
722 function is driven by a competitive disinhibitory motif that is well posed to be recruited at high-
723 speed walking. In this condition, binocular optic flow may contain prominent translational
724 components, possibly overshadowing rotational cues that are critical for course control. We
725 propose that the competitive disinhibition at the middle layer plays an important role in
726 modulating the output layer in a continuous and dynamic manner, leading to a more robust
727 estimate of the deviations from a straight course.

728 **STAR★METHODS**

729 **KEY RESOURCES TABLE**

Reagent or resource	Source	ID
Antibodies		
mouse anti-nc82 antibody	DSHB	RRID: AB_2314866
chicken anti-GFP antibody	Abcam	RRID: AB_13970
Rabbit polyclonal anti-GFP antibody	Thermo Fisher Scientific	Cat#A6455 RRID: AB_221570
rabbit anti-GABA antibody	Sigma	RRID: A2052
rabbit anti-DsRed antibody	Abcam	AB356483
goat Alexa-488 anti-chicken	Invitrogen	RRID: A11038
goat Alexa-594 anti-rabbit	Invitrogen	RRID: AB_150088
goat Alexa-633 anti-mouse	Invitrogen	RRID: AB_141431
Experimental Models: Organisms/Strains		
Drosophila UAS-2xEGFP	Bloomington Drosophila Stock Center (BDSC)	RRID: BDSC_6874
Drosophila UAS-mCD8::GFP	BDSC	RRID: BDSC_5137
Drosophila 40XUAS-mCD8::GFP	BDSC	RRID: BDSC_32195
Drosophila UAS-CD4::tdTomato	BDSC	RRID: BDSC_35837

Drosophila 20XUAS-6XmCherry in VK00018	BDSC	RRID: BDSC_52267
Drosophila 20XUAS-6XmCherry in attP2	BDSC	RRID: BDSC_52268
Drosophila 13XLexAop2-6XmCherry	BDSC	RRID: BDSC_52272
Drosophila MCFO-1[79]	BDSC	RRID: BDSC_64085
Drosophila 13XLexAop-jGCaMP7f	BDSC	RRID: BDSC_80910
Drosophila 20XUAS-jGCaMP7f	BDSC	RRID: BDSC_80906
Drosophila UAS-sytGCaMP7f	Gaby Maimon[80]	RRID: BDSC_94619
Drosophila 20XUAS-GCaMP6f, UAS-FLP	Molina-Obando et al.[81]	N/A
Drosophila hs-FLP	BDSC	RRID: BDSC_23649
Drosophila Otd-nls:FLPo	Asahina et al[82]	N/A
Drosophila pJFRC56-10XUAS>Stop>eGFPKir2.1 in attP2	Gerry Rubin	N/A
Drosophila UAS-TrpA1(B).K	BDSC	RRID: BDSC_26263
Drosophila Rdl$^{\text{FlpStop ND}}$	BDSC	RRID: BDSC_67682
Drosophila VT014724-Gal4.DBD, Rdl$^{\text{FlpStop ND}}$	this study	N/A

Drosophila GAD1-p65.AD	BDSC	RRID: BDSC_60322
Drosophila VGlut-p65.AD	BDSC	RRID: BDSC_82986
Drosophila VGlut-Gal4.DBD	Diao et al. 2015[83]	N/A
Drosophila ChaT-Gal4.DBD	BDSC	RRID: BDSC_60318
Drosophila R39E01-LexA	BDSC	RRID: BDSC_52776
Drosophila R39E01-LexA,13XLexAop2-6XmCherry	this study	N/A
Drosophila R77F05-LexA	BDSC	RRID: BDSC_54265
Drosophila R50G03-Gal4	Aljoscha Nern	N/A
Drosophila VT058487-Gal4	Vienna Drosophila Resource Center (VDRC)	N/A
Drosophila w^{1118}; R11E07-p65.AD; R77F05-Gal4.DBD	BDSC	RRID: BDSC_75953
Drosophila w^{1118}; Empty-p65.AD; Empty-Gal4.DBD	BDSC	RRID: BDSC_79603
Drosophila R23C12-p65.AD	BDSC	RRID: BDSC_70130
Drosophila R25F07-p65.AD	BDSC	RRID: BDSC_70622
Drosophila R27B03-p65.AD	BDSC	RRID: BDSC_70164

Drosophila R50G03-p65.AD	Aljoscha Nern	N/A
Drosophila VT014724-p65.AD	BDSC	RRID: BDSC_72019
Drosophila VT039047-p65.AD	BDSC	RRID: BDSC_73268
Drosophila VT040346-p65.AD	BDSC	RRID: BDSC_74542
Drosophila VT045281-p65.AD	BDSC	RRID: BDSC_75164
Drosophila R32A11-Gal4.DBD	BDSC	RRID: BDSC_69228
Drosophila R39E01-Gal4.DBD	BDSC	RRID: BDSC_70217
Drosophila R50G03-Gal4.DBD	Aljoscha Nern	N/A
Drosophila VT014724-p65.DBD	BDSC	RRID: BDSC_72146
Drosophila VT019845-Gal4.DBD	BDSC	RRID: BDSC_73315
Drosophila VT038829-Gal4.DBD	BDSC	RRID: BDSC_73679
Drosophila VT039047-Gal4.DBD	BDSC	RRID: BDSC_73724
Drosophila VT045281-Gal4.DBD	BDSC	RRID: BDSC_72221
Drosophila VT049923-Gal4.DBD	BDSC	RRID: BDSC_73921
Software and Algorithms		
MATLAB	MathWorks, Inc.	RRID:SCR_001622
R	Open-source	RRID:SCR_001905

natverse[84] (R package)	Open-source	https://github.com/natverse
ScanImage	Vidrio Technologies	RRID:SCR_014307
Gephi	Open-source	RRID:SCR_004293
Fiji	Open-source	RRID:SCR_002285
CATMAID	Open-source	RRID:SCR_006278

730 **CONTACT FOR REAGENT AND RESOURCE SHARING**

731 All data and analysis code are available upon request directed to Eugenia Chiappe
732 (eugenia.chiappe@neuro.fchampalimaud.org).

733 **EXPERIMENTAL MODEL AND SUBJECT DETAILS**

734 **Drosophila husbandry**

735 *Drosophila melanogaster* were reared on a standard fly medium and kept on a
736 12hr light/12hr dark cycle at 25 ºC. All experiments were performed with 2-to-4-days
737 old flies. Calcium imaging experiments were carried out with female and behavior
738 experiments with male flies. The complete set of transgenic flies and their specific
739 sources are listed in the *Key Resources Table*. Full genotypes of flies used in each
740 experiment are described in **Supplementary Table 3**.

741 **METHOD DETAILS**

742 **Generation of recombinant lines**

743 For the R39E01-LexA,13xLexAop-6xmCherry recombinant, transgenic lines
744 carrying R39E01-LexA and 13xLexAop-6xmCherry were crossed according to

745 standard procedures. Putative recombinant progeny was scored based on eye color
746 and ectopic mCherry labeling in the ventral cuticle and verified by immunostaining.
747 For the VT014724-p65.DBD, Rdl^{FlpStopND} recombinant, we could not use eye
748 color since FlpStop cassette does not contain the *mini-white* gene. We generated
749 stable lines from single progeny and verified recombinant lines using PCR, with
750 primers targeting the FLPStop cassette in the ND orientation as in[53].

751 **EM datasets and neuron identification**

752 **EM datasets**

753 Two different EM datasets were used: A full female adult *Drosophila* brain
754 imaged using serial section transmission EM (FAFB[40]) and another, dense
755 reconstruction of a partial adult female brain imaged using FIBSEM (focused ion-beam
756 scanning electron microscopy), referred to as Hemibrain[42]. In FAFB, neuron skeletons
757 were either manually traced using CATMAID[85,86], following the procedure described
758 in[40] or automatically segmented within the FlyWire[41] environment together with
759 chemical synapse predictions[87]. None of the EM datasets contain information about
760 electrical synapses (i.e., gap junctions).

761 **Neural reconstructions**

762 Manual tracing of neurons for 'identification' and for 'completion' has been done
763 in FAFB as described in[88]. Briefly, reconstructing the full arbor of a neuron results in
764 tracing for 'completion', while tracing the soma and the major axonic and dendritic
765 branches that contain microtubules results in tracing for 'identification'. Tracing for
766 identification saves considerable tracing time by leaving out the many small,
767 microtubule-less branches called twigs. This strategy is often enough to uniquely

768 identify a neural class. For many FAFB neurons, we were able to readily obtain
769 complete reconstructions in FlyWire with small differences in their twigs. Some
770 neurons, however, were badly segmented in earlier instances of FlyWire and had to
771 be reconstructed manually in FAFB. For example, DNp15 neurons have a darker
772 cytosol and very striated dendritic branching, which resulted in incomplete automatic
773 segmentation and connectivity in FlyWire and Hemibrain datasets. Therefore, we
774 manually traced Right DNp15 for completion and performed input profile analysis on
775 the FAFB dataset (**Fig. 2-S3f**). HS, VS and H2 cells were all traced to completion.
776 Strong LPTC partners were traced for identification, most of which were then traced
777 to completion.

778 A recent connectome analysis of the three EM datasets found that the FAFB
779 dataset is left-right inverted[89]. This means the Right hemisphere neurons we
780 reconstructed in FAFB/FlyWire are actually the Left neurons in real world coordinates.
781 Since inter-hemisphere connectivity is highly stereotyped within and across EM
782 datasets[89], and doesn't affect any of the results we present here in this study, we
783 retain the inverted naming of neurons reconstructed in FAFB. This allows for a more
784 intuitive comparison with the Hemibrain dataset, which largely encompasses the Right
785 side of the brain.

786 **Tracing synaptic connections**

787 In addition to their anatomy, we have tagged the locations of all incoming
788 (postsynaptic) and outgoing (presynaptic) chemical synapses of HS, VS, H2 cells and
789 several classes of strong LPTC partners in FAFB. As a rule, we tagged all synaptic
790 connections between any pair of traced neurons. Therefore, even if a neuron does not

791 have all their synapses tagged, we obtain the total number of synaptic connections
792 between all neurons in our FAFB dataset, provided they are fully, or near-fully traced.

793 **Selection of LPTC partners to reconstruct**

794 We traced all HS, all H2 and >90% of VS inputs for identification (**Fig. 1-S2c**).
795 For LPTC outputs, which are ~10x more numerous than inputs, we chose a pseudo-
796 random sampling approach. In FAFB, most of the strongly connected partners make
797 multiple axo-dendritic connections around the same presynaptic bouton. We focused
798 on neurons that send multiple dendrites to LPTCs within a small area by visual
799 inspection. We then prioritized tracing these 'putative strong' partners for identification.
800 In addition, we checked the strongest LPTC partners in Hemibrain and FlyWire
801 datasets and reconstructed them in FAFB if they weren't traced for identification
802 already. This allowed us to reconstruct all of the strongest LPTC partners with minimal
803 manual tracing.

804 **EM to Light Microscopy (LM) matching**

805 We used natverse R libraries[84], in particular *templatebrains* and *rcatmaid* to
806 register FAFB neurons onto a common template (JFRC2010) that's used in large
807 driver line libraries curated by the Janelia FlyLight team[90–92]. We then transformed our
808 aligned FAFB skeletons onto a 2-D ColorMIP image[93] and ran a similarity search
809 between our neurons and Gal4 lines within FlyLight. Gal4 lines with high similarity
810 were shortlisted by manual inspection. The shortlisted lines were then used in
811 combinations to generate the Split-Gal4 lines with sparse expression[94]. Stability and
812 sparseness of each split combination was assessed by checking GFP expression of
813 several brains under a confocal microscope.

814 **Immunohistochemistry**

815 **Immunostainings and microscopy**

816 2-4 days old adult *Drosophila melanogaster* brains were dissected in
817 phosphate buffer saline (PBS). Immunostaining protocol was slightly modified from[95]
818 as follows: After dissection, brains were fixed with 4% paraformaldehyde (PFA)
819 diluted in PBS for 20 minutes in room temperature (or 1 hour on ice). Before the
820 application of the primary antibodies, brains were incubated for 15 minutes in 10%
821 normal goat serum (or 1 hour in 5% normal goat serum) with 0.1% Triton X-100 in
822 PBS.

823 For checking GFP and GCaMP expression, Chicken anti-GFP (Abcam, CAT
824 #ab13970, 1:1000 dilution) was used with Mouse anti-nc82 (Developmental Studies
825 Hybridoma Bank, 1:10 dilution). In flies that additionally express TdTomato or
826 mCherry, Rabbit anti-DsRed (Abcam, CAT #ab356483, 1:500) was also used. For
827 GABA stainings, Chicken anti-GFP was used together with Rabbit anti-GABA (1:100;
828 Sigma-Aldrich CAT #A2052). Secondary fluorescent antibodies were AlexaFluor594
829 Goat anti-Rabbit (Abcam, CAT #ab150088, 1:500), AlexaFluor488 Goat anti-Chicken
830 (Abcam, CAT #ab150173, 1:500), AlexaFluor633 Goat anti-Mouse (Life
831 Technologies, CAT #A-21050, 1:500). In a small number of immunostainings, Rabbit
832 anti-GFP and AlexaFluor488 Goat anti-Rabbit were used instead.

833 Confocal sections were acquired using a Zeiss LSM710 confocal microscope
834 at 1 or 2 μm intervals and maximum projections of image stacks were performed in
835 Fiji/ImageJ (https://imagej.net/software/fiji/).

836 **Calcium Imaging**

837 **Fly preparation for immobilized calcium imaging**

838 2-4 days old adult female flies were used in all experiments. To keep their body
839 size relatively constant, 2-6 flies were anaesthetized with CO_2 after eclosion and
840 housed in vials. On the day of imaging, to minimize the potential influence of sensory
841 reafference signals coming from the limbs, flies were cold-anaesthetized, and their
842 legs were removed using fine forceps from the femur-tibia joint for the forelegs and
843 coxa-femur joint for the middle and hind legs. The femur of the forelegs were kept
844 intact since it proved difficult to reliably wax the coxa without waxing the eyes and the
845 proboscis. Openings in all the legs were then covered with beeswax. Proboscis was
846 gently extended using fine forceps and waxed from below to minimize the movement
847 of the brain during imaging. The fly was mounted on a custom-made physiology holder
848 by temporarily pinning the thorax onto a small tungsten wire (A-M Systems #716100)
849 using UV-cured glue (Bondic). The mounting is aided by a custom-built
850 micromanipulator and a triple camera array to position the head in the same
851 orientation across flies. After each experiment, high resolution images of the fly head
852 from the side and bottom were taken to measure the head pitch, yaw and roll angles
853 as described in[50]. Once the desired head orientation is achieved, the fly head and the
854 body were waxed onto the physiology holder, and the UV-glued pin was removed. The
855 cuticle from the back of the head was removed with extra sharp forceps (Dumont 5SF).
856 Fat body tissues were removed by gentle suctioning while trachea and the muscles 1
857 and 16 of the fly head were removed by fine forceps. In this preparation, flies have no
858 mobility in their legs and proboscis, very limited mobility in their wings and abdomen,
859 and high mobility in their halteres and antennae.

860 **Imaging setup**

861 Flies ready for imaging were mounted under an upright microscope (Movable
862 Objective Microscope, Sutter) with a 40× water-immersion objective lens (CFI Apo
863 40XW NIR, Nikon). Calcium imaging was performed with a custom-built galvo-galvo
864 2-photon laser scanning system. We used a Chameleon Ultra II Ti-Sapphire
865 femtosecond laser (Coherent) tuned to 930 nm for GCaMP and tdTomato excitation
866 (6 mW under the objective lens) and 780 nm for mCherry excitation when available.
867 The longer excitation wavelength is not visible to the fly. Emission was collected on
868 GaAsP PMT detectors (Hamamatsu, H10770PA-40) through a 535/50 nm bandpass
869 filter for the green channel and 605/70 nm for red channel (Chroma). A 128x128 pixels
870 slice image was acquired with ScanImage at the dorsal part of the posterior slope,
871 where the axon terminals of all neurons that were imaged overlap. To record activity
872 in a consistently large region across different cell types, the acquisition frame rate
873 varied between 12.2-15.0 Hz. When mCherry or tdTomato was co-expressed with
874 GCaMP, higher resolution 3D z-stacks were taken of the imaged regions before or
875 after each experiment. The external solution, which perfused the preparation
876 constantly in room temperature, contained 103 mM NaCl, 3 mM KCl, 5 mM TES, 8
877 mM D-trehalose, 10 mM D-glucose, 26 mM $NaHCO_3$, 1 mM NaH_2PO_4, 4 mM $MgCl_2$
878 and 2 mM $CaCl_2$ in MilliQ water (270–275 mOsm) and was bubbled with 95% O_2 / 5%
879 CO_2 (pH ~7.3).

880 **Visual display**

881 The visual display consists of a 32 × 96 array of blue light-emitting diodes
882 (LEDs, 465 nm, Bright LED Electronics) that are modeled after Generation 3 (G3)

883 modular display[96] with four layers of blue filter (Rosco R385) to minimize light leaking
884 into photomultiplier tubes used in calcium imaging. For a centrally positioned fly, its
885 visual field subtended 216° in azimuth and 72° in elevation (pixel size of 2.25°). In an
886 initial set of experiments, we prepared flies for imaging and measured the head pitch
887 angle as described in[50]. The display was tilted 74° relative to the horizon to match the
888 average pitch angle of the imaged flies.

889 **Visual stimuli**

890 Starfield stimuli[97] were generated using MATLAB (MathWorks, Natick, MA)
891 scripts (from https://github.com/misaacson01/Motion_Maker_G4), which were slightly
892 modified to be compatible with the G3 display. We virtually extended our display onto
893 a 2D spherical volume and populated this volume with 500, equally sized dots (5° solid
894 angle diameter) at random and uniformly distributed positions. We illuminated the
895 pixels on the LED display that overlapped with the dots in this spherical volume.
896 Instead of having fully on/off edges, we used 16 gray-scale intensity levels which
897 allowed for edges in visual patterns to appear to move more smoothly across frames.
898 This increases the apparent resolution of the display while minimizing motion-
899 independent flicker responses in recorded neurons. All dots had a nominal contrast of
900 100%.

901 Each trial consists of an identical, stationary visual pattern shown to the fly,
902 followed by clockwise and counterclockwise movements of the pattern in a particular
903 body axis of rotation (pitch, yaw, and roll) or movements of the pattern in translational
904 axes (thrust and sideslip) that lasts for 2 seconds, flanked by stationary periods. Each
905 trial lasted for 13 seconds (still-motion-still-motion-still for 2-2-5-2-2 seconds) with 5

906 seconds of inter-trial interval where the visual display was unlit (dark). See
907 **Supplementary Video 1** for all optic flow patterns. In speed tuning experiments, only
908 one direction of motion was presented, as such, trials lasted for 6 seconds (still-
909 motion-still for 2-2-2 seconds). See **Supplementary Video 2** for speed tuning stimuli.
910 Every visual pattern was shown 3-12 times for each fly, and the order of the trials were
911 randomized.

912 **Choice of calcium indicators**

913 We initially tested several GCaMP variants to reliably record calcium activity
914 across all the cell types imaged in this study. We found sytGCaMP7f[80] to give us the
915 strongest signal-to-noise ratio across most cell types. In addition, sytGCaMP7f
916 guarantees imaging from the axon terminals, which allowed us to confidently
917 distinguish calcium activity coming from Right bIPS axons versus Left bIPS dendrites.
918 Therefore, we used sytGCaMP7f in most of our recordings. DNp15 does not have
919 axon terminals in the brain, so we used cytoplasmic GCaMP7f[98] instead. In FLPStop
920 experiments we used cytoplasmic GCaMP6f[99] which was readily recombined with
921 UAS-FLP and used in FlpStop experiments previously[81]. In these experiments, we
922 distinguished dendritic and axonic signals in bIPS using the anatomical landmarks
923 provided by TdTomato expression as well as the direction selectivity of the recorded
924 ROIs.

925 **Data acquisition and alignment for imaging**

926 Before quantifying fluorescence intensities, imaging frames were motion-
927 corrected in MATLAB by translating each frame in the x and y plane using efficient
928 subpixel image registration[100] to match the time-averaged template from that session.

929 Multiple recordings from the same fly were registered to the same template if the
930 positional shift between recordings was small. In a small number of flies the analysis
931 was performed on raw image traces, where the movement correction resulted in
932 abnormal shifts of imaging frames in most of the trials despite negligible brain
933 movement. All trials where the imaged neurons move out of the imaging plane were
934 discarded.

935 **Behavior**

936 **Exploratory walking arena**

937 The virtual reality setup used in the exploratory walking experiments has been
938 previously described[39]. Briefly, single 2-4 days old male flies with their wings clipped
939 since eclosion walked freely in a 90 mm circular arena with heated walls. We projected
940 an array of random dots that provide prominent visual feedback and translate together
941 with the fly using real-time tracking of the fly's center of mass and orientation.

942 To label single bIPS or DNp15 cells, flies were placed under 30°C heat shock
943 for up to 15 minutes after their wings were removed post-eclosion. The brains of these
944 flies were dissected immediately after each experiment to confirm cell labeling.

945 **Agent fly simulations**

946 A simulated rigid-body agent moved forward or executed a saccade in
947 alternating activity and immobility intervals (**Fig. 5-S1d**). The distribution of the length
948 of activity bouts was similar to the real flies' distribution[39]. The agent explored a
949 simulated 90 mm circular arena with hot walls. Saccades were modeled as highly
950 stereotyped rapid events in the angular velocity of the agent. The probability and
951 amplitude/direction of a saccade depended on the distance to the arena wall. The time

intervals within an activity bout without saccades were considered forward runs. Forward runs had constant translational speed (20 mm/s) except in **Fig. 5f** where the forward velocity was varied. During forward runs, non-zero slow rotations are represented by an "injected" 1/f noise (η). The size of η was scaled by the parameter 'Noise Level' (w_{noise}) to match the straightness of real flies walking in dark (**Fig. 5-S1f**).

Rotations of the agent are guided by a visual controller based on measured visual flow from both eyes. In short, four channels containing arrays of a "two-quadrant" type Hassenstein-Reichardt (HR) correlator detected self-generated visual motion cues[101]. Self-generated visual stimuli were modeled first by high-pass filtering the visual pattern at each spatial position (τ = 50ms). This was followed by a half-wave rectification step. Next, the visual signal was low-pass filtered (first order, τ = 15ms), and then multiplied with an unfiltered signal from a neighboring spatial location. This was done twice in a mirror-symmetrical manner, followed by subtraction, yielding a fully opponent direction-selective output signal, which was then scaled by the parameter 'Visual Weight' (w_{visual}) to match straightness of real flies experiencing visual motion cues (**Fig. 5-S1g**). The two eyes of the agent are represented by independent arrays of HR, each detecting progressive (FtoB) and regressive (BtoF) visual rotations. Combinations of progressive and regressive signals were then used to simulate the response profiles of HS and H2 cells.

$$HS_{right} = w_{HSPD} * FtoB_{right} - w_{HSNPD} * BtoF_{right} + w_{HSContra} * BtoF_{left}$$

$$H2_{right} = w_{H2PD} * BtoF_{right} - w_{H2NPD} * FtoB_{right} + w_{H2Contra} * FtoB_{left}$$

The weights for HS and H2 responses were adjusted based on a subset of horizontal visual motion responses obtained (**Fig. 5-S1a**). Following HS and H2, the intermediate layer of inhibitory neurons – bIPS (B) and uLPTCrns (U) was simulated according to the architecture outlined in **Fig. 5a**.

$$B_{right} = w_{HSB} * HS_{right} + w_{H2B} * H2_{left} - w_{UB} * U_{right}$$

$$U_{right} = w_{HSU} * HS_{right} + w_{H2U} * H2_{left} - w_{BU} * B_{left}$$

Like HS and H2, the weights for bIPS and uLPTCrn responses were also adjusted based on real visual responses (**Fig. 5-S1b**). Finally, all simulated neurons converge onto a simulated DNp15 modeled after the H2-HS network architecture in **Fig. 2**.

$$DNp15_{right} = w_{HSp15} * HS_{right} + w_{H2p15} * H2_{left} - w_{Up15} * U_{right} - w_{Bp15} * B_{left}$$

The weights for DNp15 were adjusted to match the measured horizontal visual motion responses in **Fig. 1-S1c** by iteratively changing the weights of the input layer (HS and H2) and then changing the weights of the intermediate layer (B and U). The final table of weights is presented in **Fig. 5-S1c**.

The agent's rotation depends on the activity difference between Left and Right DNp15.

$$V_{angular}\ (°/s) = w_{visual} * \left(DNp15_{right} - DNp15_{left}\right) + w_{noise} * \eta$$

Where w_{visual} , w_{noise} and η correspond to the visual weight, noise level and injected 1/f noise, respectively. In the current framework, neuronal silencing was mimicked by turning the signal from specific neurons to zero, while activation was mimicked by turning the signal from specific neurons to 0.1. Asymmetry indices (AI) were calculated by comparing the activity between left and right neurons for each neural population:

996 $$AI_{neuron} = \frac{|Neuron_{left} - Neuron_{right}|}{|Neuron_{left}| + |Neuron_{right}|}$$

997 **Data analysis**

998 **EM connectivity matrices and synaptic clustering**

999 We used *natverse*[84] R libraries to load HS, VS and H2 cells from FAFB and
1000 prune their dendritic arbor in the optic lobes, leaving only the central brain projections.
1001 We then loaded the list of all their synaptic partners, and together with HS, VS and H2
1002 cells, we generated an all-by-all connectivity matrix where each point corresponds to
1003 the number of synapses from a row neuron to a column neuron.

1004 To cluster the neurons that are more closely connected with each other, we
1005 first summed input and output synapses between each pair of neurons, thereby
1006 generating a symmetric connectivity table. We then binarized this table, setting all non-
1007 zero connections to 1. This prevents very strong pairwise connections to take over
1008 and distort network clustering. Conversely, it increases the weight of the weakest
1009 connections (i.e., <5 synapses). Therefore, we convert all weak connections to zero
1010 before binarization. We compute the distance matrix using this binarized connectivity
1011 and perform hierarchical clustering with Ward's method to generate the connectivity
1012 dendrogram in **Fig. 2-S1**. The dendrogram was used to reorder the initial connectivity
1013 matrix where neurons that are clustered together are placed next to each other. We
1014 also ran the same clustering analysis without binarization nor removing weak partners
1015 (**Fig. 2-S2**) to confirm the broad network structure does not critically depend on these
1016 subjective parameters.

1017 **Network connectivity graphs**

1018 After generating the clusters, neurons within each cluster are loaded in
1019 CATMAID[86]. Neurons that belong to the same class (largely based on anatomy) are
1020 grouped together, generating a graph structure where each node is a neuron class
1021 and directed edges between nodes represent the number of synaptic connections.
1022 The adjacency matrix of this graph structure is then imported to Gephi where the edge
1023 and node parameters (color, size etc.) are adjusted for better visualization. The end
1024 point shape of each edge was determined by their predicted primary
1025 neurotransmitter[52].

1026 To measure the prominence of a neural class within each subnetwork, we
1027 plotted the weighted degree, which is the total number of incoming and outgoing
1028 synapses for each node inside that subnetwork (**Fig. 2b**).

1029 **Anatomical clustering of LPTC inputs**

1030 To quantify the anatomical similarities among LPTC input cell types (**Fig. 2-**
1031 **S3d**), we performed NBLAST[102] on the main backbone (primary neurite tracts with the
1032 primary dendrites) of LPTC input neurons. The smallest distal dendrites (twigs) were
1033 removed since they are highly variable and make NBLAST less sensitive to the
1034 stereotyped features of cells. Hierarchical clustering was then performed on Euclidean
1035 distance matrices of NBLAST scores using Ward's method.

1036 **Synaptic input profiles**

1037 To plot the neuropil input profile of LPTC input neurons (**Fig. 2-S3e, Fig. 3c**),
1038 we first obtained the list of upstream partners from FlyWire for each cell type. We only
1039 analyzed predicted synaptic sites with a cleft score of >50 to minimize false positives.
1040 We defined the input neuropil of each upstream cell as the brain region that houses

1041 most of their postsynaptic (dendritic) sites. Upstream cells that lack a soma or have
1042 less than 200 postsynaptic sites were visually inspected. The ones that project to the
1043 neck connective were scored as VNC/Neck. The remaining fragments without a cell
1044 soma were excluded from the analysis. For the DNp15 input profile (**Fig. 2-S3f**) we
1045 fully reconstructed Right DNp15 in FAFB and manually tagged all its synapses since
1046 it was badly segmented in FlyWire. We then traced ~89% of its synaptic partners for
1047 identification and defined their primary input neuropil. To plot the neurotransmitter
1048 input profile of bIPS (**Fig. 4a**) we regrouped the list of Right bIPS input neurons based
1049 on their predicted neurotransmitter[52].

1050 **Distance-to-root and inter-synaptic distance analyses on bIPS**

1051 We retrieved the spatial distribution of Right bIPS inputs from FAFB using
1052 *natverse* R libraries[84]. The location of each input synapse from Right HS, H2rn,
1053 uLPTCrn and Left H2 cells were projected onto a graph representation of bIPS neuron
1054 using *nabor* library. We defined the root point of bIPS as the soma-axon-dendrite
1055 junction, which is where all the dendritic arbors of bIPS converge before crossing the
1056 midline (**Fig. 4-S2a**). We then computed the geodesic distance between each input
1057 synapse and the root point using *igraph* library (**Fig. 4-S2b,c**). This analysis is loosely
1058 based on the electrotonic distance analysis within EPG neurons performed by Hulse
1059 et. al.[103]. Geodesic distances between H2rn inputs and the nearest H2 or HS input
1060 were calculated in a similar manner (**Fig. 4-S2d**).

1061 **Proportion of local circuitry motifs**

1062 The non-random locations of bIPS input synapses suggest they may be
1063 organized in distinct microcircuits as they contact bIPS. We assumed only one

1064 synaptic input from a presynaptic cell takes part in a microcircuit. We therefore defined
1065 1.865 μm as the maximum inter-synapse distance (**Fig. 4-S2d**, black line) based on
1066 the distances between H2rns with H2. We then counted the number of times a cell
1067 type (cell X) forms a microcircuit with H2 (**Fig. 4-S2e** and **4-S2g**) or HS (**Fig. 4-S2f**
1068 and **4-S2h**) as they give input to bIPS (**Fig. 4-S2d-f**) or DNp15 (**Fig. 4-S2f-h**),
1069 normalized by the total number of occurrences per motif.

1070 **Calcium responses to visual motion**

1071 After each imaging session, we manually defined regions of interest (ROI) that
1072 correspond to the axon terminals or dendrites of recorded neurons. For lines that label
1073 single neurons (e.g., H2, bIPS), only one ROI was defined. For lines that label multiple
1074 neurons, multiple ROIs were first defined. After confirming the visual responses of
1075 different ROIs were not qualitatively different, we chose a single ROI with the largest
1076 signal-to-noise ratio to represent the cell type. As such, we recorded the responses of
1077 no more than two ROIs per fly, one per hemisphere.

1078 To calculate calcium evoked responses in these ROIs, we calculated mean
1079 pixel intensity (fluorescence) for each trial (F). Baseline fluorescence (F_0) was defined
1080 as the F value of the last second before the first visual motion presentation. Change
1081 in calcium response was measured as:

1082 $$\Delta F = F - F_0$$

1083 Since $\Delta F/F$ measurements of calcium activity could create positive artifacts
1084 following negative deviations from baseline observed in several cell types we
1085 imaged[104], we instead Z normalized the ΔF data to compare optic flow responses
1086 within and across cell types. We downsampled the imaging data from each fly to the

1087 lowest recorded frame rate (12.2Hz). Recordings from left hand side cells were flipped
1088 to match the responses from right side recordings (and vice versa for H2 recordings).
1089 Matching is done by converting the stimulus identity (e.g. roll CW, pitch CW and yaw
1090 CW) into its midline-symmetric version (roll CCW, pitch CCW and yaw CCW), similar
1091 to what is described in Weir et al.[97]. Finally, all repetitions of a given stimulus were
1092 averaged to get a single mean response per stimulus per ROI.

1093 **Optic flow response indices**

1094 To measure the relative sensitivity of a neuron to a particular pattern of optic
1095 flow, we calculated the response as the area under the curve (auc) during the entire
1096 2 seconds of visual motion stimulation or calculated the mean response within the last
1097 200 ms of visual motion (peak). The preferred (PD) and non-preferred (NPD) direction
1098 of visual motion for all axes of movement were defined based on Right HS cell
1099 responses. Optic Flow (OF) responses (**Fig. 3c**) were plotted as the difference
1100 between calcium responses of the preferred (PD) and non-preferred (NPD) direction
1101 related to a given stimulus (e.g., CW minus CCW). The OF responses in **Fig. 3d** were
1102 normalized by the peak OF response per ROI.

1103 To measure the discrimination index (DI), we first calculated the peak OF
1104 response for a given optic flow pattern (e.g., Yaw). Here, PD and NPD responses were
1105 defined per cell type:

1106 $OF_{Yaw} = Peak_{PD} - Peak_{NPD}$

1107 The DI between two optic flow patterns (e.g., Progressive and Yaw) is
1108 calculated as the difference between OF values divided by the sum of the absolute
1109 OF values:

1110 $$DI = \frac{OFProg - OFYaw}{||OFProg|| + ||OFYaw||}$$

1111 **Classification of walking paths, walking straightness, and angular deviations**

1112 Walking paths are classified into spike-like saccadic events that correspond to
1113 rapid turns and forward segments as described in Cruz et al.[39]. Straightness of forward
1114 segments are calculated by first measuring local deviations from an ideal path within
1115 a running window of 333 ms for each point of the fly trajectory. Straightness is defined
1116 as the total distance traveled within each window divided by the sum of local
1117 deviations. Angular path deviation for each forward segment is defined as the
1118 cumulative angular deviation of the body divided by the total distance traveled.
1119 Angular bias is the binarized version of angular path deviation (**Fig. 1g, 5-S1e**).

1120 **QUANTIFICATION AND STATISTICAL ANALYSIS**

1121 **Statistics**

1122 We performed a two-sided Wilcoxon rank-sum (here, abbreviated as MWW)
1123 test for comparisons between two independent groups with Bonferroni correction for
1124 multiple comparisons where applicable.

1125

1126 **DATA AND CODE AVAILABILITY**

1127 Analysis codes and data in this paper are available upon request to the Lead Contact.

1128 ## Supplementary figure and video legends

1129 **Figure 1-S1: DNp15's responses to optic flow and their effect on body saccades** (**a**)
1130 Mean responses to rightward horizontal binocular optic flow moving in different speeds for
1131 Right HS (magenta) and right DNp15 (olive). The speed of the stimuli presented in the other

1132 panels of this figure, and of the rest of the figures in this study is highlighted in red. Gray
1133 shaded area indicates the duration of visual stimulation. Each trace corresponds to the grand
1134 mean of z-scored calcium responses. The mean response to 5-10 repetitions per stimulus
1135 from a single region of interest (ROI) at the axon terminals per fly was used to compute the
1136 garnd mean. Shaded area represents standard error of the mean. (**b**) Speed tuning curves
1137 calculated as the area under the curve during stimulus motion, normalized by the maximum
1138 response per ROI. (**c**) Responses of HS and DNp15 cells to different binocular and monocular
1139 optic flow stimuli. FTB= front-to-back, BTF= back-to-front visual motion (**d**) Top, schematic
1140 illustrating directions of body translations and the resulting optic flow without rotating the head.
1141 Bottom, right HS (magenta) and DNp15 (olive) responses to translational optic flow. (**e**)
1142 Discrimination index for HS and DNp15 between different patterns of optic flow. Each circle
1143 represents an individual ROI. Colored horizontal line and black vertical line represents mean
1144 and 95% CI. (HS: N=12 flies, n=16 ROIs, DNp15: N=6 flies n=7 ROIs, *P < 0.05; **P < 0.01
1145 ***P < 0.001, Wilcoxon's rank-sum test). (**f**) Immunostainings showing the stochastic
1146 expression of kir2.1:GFP in both, none, left or right DNp15 cells. (**g**) Effect of the stochastic
1147 silencing on saccade bias (see **Methods**). Number of flies per condition, none n=25; both
1148 n=31; left n=22; right n=22. The size of circles indicates the number saccades.

1149 **Figure 1-S2. LPTC axon terminals send outputs to and receive inputs from central**
1150 **neurons** (**a**) Left, schematic of the data coverage of the fly brain (dark gray) available from
1151 two large-scale fly brains imaged under EM resolution, FAFB and Flywire (top) and Hemibrain
1152 (bottom). Right, reconstructions of the right HSE cell in the three EM datasets. FAFB contains
1153 skeletonized neurons while FlyWire and Hemibrain provide volumetric reconstructions of cells.
1154 Postsynaptic (input) and presynaptic (output) site locations are marked with cyan and red
1155 dots, respectively. (**b**) Example EM section at the axon terminals of HSE (yellow) and a
1156 recurrent synaptic partner (green). Arrowheads indicate the location of presynaptic active

1157 zones. Scale bar, 1 μm. (**c**) Top, number of inputs (i.e., upstream partners) for H2, HS and
1158 VS cell classes in the posterior slope region of the fly central brain. Numbers in parentheses
1159 indicate number of cells present in each cell class. Presynaptic neurons traced for
1160 identification are colored based on the EM dataset. Synapses from untraced neurons are
1161 colored in gray. Bottom, same as Top, but for outputs (i.e., downstream partners). (**d**) Top,
1162 distribution of the number of synaptic connections between LPTCs and their inputs. Color
1163 code indicates EM dataset and tracing status. Each distribution is normalized by total number
1164 of synapses. Inset shows a zoomed version of the region outlined by the dashed rectangle.
1165 Neurons with more than 10 synapses (black line) are considered strong inputs. Bottom, same
1166 as top, but for LPTC outputs. Neurons with more than 35 synapses (black line) are considered
1167 strong outputs.

1168 **Figure 1-S3: LPTCs have few strong, and many weak synaptic partners.** (**a**) Number of
1169 inputs H2 (top), HS (middle), and VS (bottom) cells receive from central neurons. Presynaptic
1170 central neurons are ordered from strongest to weakest. Color code indicates EM data- set.
1171 Inset, input numbers normalized by the strongest input cell (**b**) same as, **a**), but for LPTC
1172 outputs. (**c**) Pairwise matching of the strongest H2, HS (n=3) and VS (n=8) outputs across EM
1173 datasets. Cells are ordered based on total number of inputs they receive from each LPTC
1174 class. Matching is primarily based on a cell's anatomy, aided by its synaptic connectivity. Black
1175 lines represent matches where both pairs are within the top 10 strongest outputs in their
1176 respective EM dataset. Gray lines indicate that only one of the pairs is within the top 10.
1177 Dashed lines indicate uncertain matching due to the incomplete or bad segmentation in
1178 Hemibrain. See **Supplementary Table 1** for the cell identities.

1179 **Figure 2-S1: The synaptic connectivity matrix among LPTC and their partners is**
1180 **structured.** The synaptic connectivity matrix of HS, VS, H2 cells and their strongest synaptic
1181 partners in the central brain. Neurons are colored based on anatomical similarities, color code

1182 as in **Fig. 2** (see **Supplementary Table 2** for the complete list of neurons and nomenclature).
1183 The number of synaptic connections between pairs is indicated by the grayscale color code.
1184 In addition, connections are either colored red or blue based on the hierarchical clus- tering
1185 analysis, which represent whether connections belong to the H2-HS or VS networks,
1186 respectively (dendrogram, see **Methods**).

1187 **Figure 2-S2: The structure of the connectivity matrix is largely unaffected by synaptic**
1188 **thresholds.** The pairwise synaptic connectivity matrix among HS, VS, H2 cells their synaptic
1189 partners in the central brain, without applying any thresholds to the connectivity strength (232
1190 neurons total). Like in **Figure 2-S1**, number of synaptic connections between pairs is indicated
1191 by the grayscale color code. The dendrogram shows the hierarchical clustering analysis of
1192 the connectivity matrix (see **Methods**). Colored lines in the dendrogram indicate the cluster
1193 which the neuron belongs to in **Figure 2-S1**. The location of HS, H2 and VS cells within the
1194 matrix is highlighted.

1195 **Figure 2-S3: The middle layers of the H2-HS and VS networks are characterized by**
1196 **distinct classes of interneurons.** (**a**) Percentage of total number of inputs to the left H2 (left),
1197 right HS (middle) and right VS cells (right) grouped by class (color code). LPTC inputs that do
1198 not belong to the five major interneuron classes are grouped together as “other”. (**b**) Posterior
1199 view of the morphology of single cell examples from each LPTC input interneuron class. Red
1200 and cyan dots mark the location of pre- and postsynaptic sites, respectively. Regions of
1201 innervation are outlined in gray. (**c**) Anatomical reconstructions of bilateral populations of
1202 neurons per class. Top, posterior views; bottom, dorsal views. Each neural class forms a
1203 bilateral, mirror symmetric population (**d**) NBLAST-based anatomical clustering of the main
1204 backbones of the LPTC input interneurons. (**e**) Left, schematic of the fly brain with key
1205 neuropils sending projections to LPTC inputs. Right, percentage of total synaptic inputs of
1206 bLPTCrn (right) and cLPTCrn (right) cells in FlyWire grouped by the main brain regions where

1207 they receive dendritic input. (**f**) Same as **e**) but for the right DNp15 from FAFB. Input neurons
1208 from H2-HS network shown in **Figure 3a** are highlighted with colored lines. IPS - inferior
1209 posterior slope; SPS - superior posterior slope; GNG - gnathal ganglion; LOP - lobula plate;
1210 ME - medulla; VNC - ventral nerve cord.

1211 **Figure 3-S1: Transgenic lines used to gain access to H2-HS network neurons. (a)**
1212 Maximum intensity projections of transgenic lines labeling H2-HS network neurons. The
1213 specific cell class is indicated above each image (see **Methods** for a list of the transgenic
1214 lines). Neuropil (nc82) staining is shown in magenta, membrane targeted GFP or cytoplasmic
1215 GCaMP expression is shown in green. (**b**) Single-cell labeling using Multicolor FlpOut (MCFO)
1216 shows that the LPTCrn-Split Gal4 line contains both cLPTCrn (top) and uLPTCrn (bottom)
1217 cells. (**c**) Maximum intensity projections of transgenic lines that are heterozygous (left) or
1218 homozygous (right) mutants for *Rdl* in bIPS neurons. Neuropil staining is shown in magenta,
1219 cytoplasmic GCaMP expression is shown in green, TdToma- to expression, resulting from a
1220 successfully disruption of the Rdl gene with the FLP-Stop cassette, is shown in red. Note that
1221 one copy of Rdl-FlpStop gene is enough to express TdTomato in bIPS. Scale bar for all
1222 panels: 100 μm.

1223 **Figure 3-S2: Responses of H2-HS network neurons to different optic flow patterns.** (**a**)
1224 Top, schematics illustrating rotations of the fly's body along six degrees of freedom. Bottom,
1225 calcium responses to the corresponding visual consequences of the body rotations from the
1226 fly's perspective in right HS (magenta), left H2 (blue), right bIPS (green), right H2rn (red) and
1227 right uLPTCrn (orange) cells. Gray shaded area shows the window of stimulation. Each trace
1228 corresponds to the grand mean± SEM (shade) of z-scored calcium responses obtained across
1229 flies. In each fly, mean responses were obtained from 5-10 repetitions of per stimulus from a
1230 single ROI at the axon terminals of the cells. (**b**) Left, responses of right HS, left H2, right
1231 bIPS, right H2rn and right uLPTCrn to horizontal optic flow moving CW at the indicated

1232 speeds. The speed of the rotational and translational optic flow presented in other figures is
1233 highlighted in red. Calcium responses are plotted the same way as in **a**). Right, speed tuning
1234 curves for each cell type. (**c**) Same as **a**), but for monocular stimuli. FTB= front-to-back, BTF=
1235 back-to-front visual motion (**d**) Same as **a**), but for binocular symmetric optic flow. For all
1236 panels: HS: N=12 flies n=16 ROIs, H2: N =8 flies n=11 ROIs, bIPS: N=15 flies n=16 ROIs,
1237 H2rn: N=5 flies n=8 ROIs, uLPTCrn: N=5 flies n=5 ROIs.

1238 **Figure 3-S3: Responses of H2-HS network neurons to translational optic flow** (**a**)
1239 Schematic illustrating possible body traveling directions (translations) and the corresponding
1240 optic flow without rotations of the head or body. (**b-f**) Calcium responses of right HS (**b**), left
1241 H2 (**c**), right bIPS (**d**), right H2rn (**e**) and right uLPTCrn (**f**) to translational optic flow patterns
1242 arranged in the same order as in **a**). Gray shaded area depicts the stimulation window. Each
1243 trace corresponds to the grand mean ± SEM (shaded area) of z-scored calcium responses
1244 obtained across flies. For each fly, mean responses to 5-10 repetitions per stimulus were
1245 obtained from a single ROI at the axon terminals. (**g**) Progressive-Sideslip discrimination index
1246 of neurons shown in panels **b-f**) (see **Methods**). Each circle represents an individual ROI.
1247 Colored horizontal line and black vertical line represents mean and 95% CI. (**h**) Same as **g**),
1248 but for Diagonal Translation vs. Sideslip discrimination index. For all panels: HS: N=10 flies
1249 n=10 ROIs, H2: N =8 flies n=9 ROIs, bIPS: N=9 flies n=9 ROIs, H2rn: N=5 flies n=8 ROIs,
1250 uLPTCrn: N=8 flies n=10 ROIs, *$p < 0.05$; **$p < 0.01$ ***$p < 0.001$, Wilcoxon's rank-sum test
1251 with Bonferroni correction for multiple comparisons).

1252 **Figure 4-S1: Central LPTC input neurons are GABAergic** (**a**) Representative confocal
1253 images showing immunoreactivity against GABA and GFP in cell bodies of each class of
1254 LPTC input neuron, as indicated on top of the images. Dashed circles outline cell bodies.
1255 Scale bar is 100 μm for full brain images and 10 μm for insets. (**b**) Reconstitution of the
1256 expression of each class of LPTCinput neurons by genetic intersection between LPTC input

1257 hemidrivers (columns) and GAD1 (top), ChaT (middle), or Vglut hemidrivers (bottom).
1258 Membrane-targeted GFP expression is shown in green, neuropil (nc82) staining is shown in
1259 magenta. Scale bar is 50 μm. Note the strong expression of each cell type under GAD1
1260 hemidriver and weak to no expression under ChaT and VGlut hemidrivers. A complete list of
1261 the genotypes can be found in **Supplementary Table 3**.

1262 **Figure 4-S2: The synaptic inputs of bIPS are organized non-randomly.** (**a**) Example of
1263 inputs to bIPS and the root point of the neuron. (**b**) Geodesic distance between bIPS root point
1264 and synaptic inputs from H2rn (n=192), HS (n=380), H2 (n=164), uLPTCrn (n=238), or a
1265 random subsample of the remaining inputs (n=192, see **Methods**). (**c**) Cumulative distribu-
1266 tions from (**b**). (**d**) Distance between an HS, H2 or other input synapse to bIPS and the closest
1267 H2rn input to bIPS. The vertical black line indicates the maximum inter-synapse distance used
1268 to defined local connectivity. (**e-h**) Proportion of connectivity motifs that involve H2 (**e,g**) or
1269 HS (**f,h**) that converge onto bIPS (**e-f**) or DNp15 (**g-h**) with an additional neuron (cell X) color
1270 coded by cell type. Schematics at the top of each panel show the three cells involved.
1271 Numbered schematics show the connectivity motif plotted per graph.

1272 **Figure 5-S1: Calibration and parameters of the visually guided agent.** (**a**) Visual
1273 responses of simulated and real HS and H2 cells for different preferred (PD), non-preferred
1274 (NPD) and contralateral (Con) weights. (**b**) Visual responses of simulated and real bIPS and
1275 uLPTCrn cells for different HS, H2 and cross-connection weights. (**c**) Final table with manually
1276 adjusted weights based on visual responses from **a**) and **b**). (**d**) Schematic of the state flow
1277 of the modeled agent, and the associated distributions for saccades (inset, top) and activity
1278 bout size (inset, bottom) estimated from the real data. (**e**) Definition of the quality parameters,
1279 straightness, path deviation and angular bias. (**f**) Simulated straightness under dark
1280 conditions, as a function of 1/f noise level. Black line represents the mean straightness
1281 observed in real flies. (**g**) Simulated straight- ness under light conditions with visual feedback,

as a function of visual weight. Black line represents the mean straightness observed in real flies. (**h**) Simulated straightness under dark (black) and light (gold) conditions for the chosen noise and visual weights. Shaded areas represent the standard error of straightness observed in real flies under light and dark conditions (Cruz et al. 2021)[39]

Figure 6-S1: Transgenic lines used in behavioral experiments (**a**) Posterior view of maximal projection stacks of three different Split-Gal4 lines labeling bIPS. Neuropil (nc82) staining is shown in magenta and membrane targeted GFP expression is shown in green. Scale bar, 200 µm. (**b**) Posterior view of maximal stack projection of example brains with stochastic silencing of bIPS. Neuropil (nc82) staining is shown in magenta and membrane-targeted, Kir2.1-bound GFP expression is shown in green. Scale bar, 100 µm. For the complete list of genotypes of all transgenic lines, please see **Supplementary Table 3**.

Supplementary video 1: Optic flow stimuli used in this study. Patterns of optic flow used in this study. Note that the LED arena is curved such that the middle of the video screen is in front of the fly while the edges are on either side of the fly (**Fig. 1c**).

Supplementary video 2: Speed tuning stimuli used in this study. Example of binocular horizontal rotational optic flow presented at different speeds.

References

1. Mahajan, N. R. & Mysore, S. P. Donut-like organization of inhibition underlies categorical neural responses in the midbrain. *Nat. Commun. 2022 131* **13**, 1–17 (2022).

2. Hu, Y. *et al.* A Neural Basis for Categorizing Sensory Stimuli to Enhance Decision Accuracy. *Curr. Biol.* **30**, 4896-4909.e6 (2020).

3. Koyama, M. & Pujala, A. Mutual inhibition of lateral inhibition: a network motif for an elementary computation in the brain. *Curr. Opin. Neurobiol.* **49**, 69–74

(2018).

4. Tihana Jovanic, A. *et al.* Competitive Disinhibition Mediates Behavioral Choice and Sequences in Drosophila Article Competitive Disinhibition Mediates Behavioral Choice and Sequences in Drosophila. *Cell* **167**, 858–870 (2016).

5. Zhao, W. *et al.* A disinhibitory mechanism biases Drosophila innate light preference. *Nat. Commun. 2019 101* **10**, 1–11 (2019).

6. Gibson, J. J. *The Perception of the Visual World. The Philosophical Review* **60**, (The Riverside Press, 1950).

7. Koenderink, J. J. Optic flow. *Vision Res.* **26**, 161–179 (1986).

8. Wurtz, R. H. Optic flow: A brain region devoted to optic flow analysis? *Curr. Biol.* **8**, 554–556 (1998).

9. Zhang, Y., Huang, R., Nörenberg, W. & Arrenberg, A. B. A robust receptive field code for optic flow detection and decomposition during self-motion. *Curr. Biol.* **32**, 2505-2516.e8 (2022).

10. Kohn, J. R., Heath, S. L. & Behnia, R. Eyes matched to the prize: The state of matched filters in insect visual circuits. *Front. Neural Circuits* **12**, 26 (2018).

11. Franz, M. O. & Krapp, H. G. Wide-field, motion-sensitive neurons and matched filters for optic flow fields. *Biol. Cybern.* **83**, 185–197 (2000).

12. Barnes, W. J. P., Horseman, B. G. & Macauley, M. W. S. The Detection and Analysis of Optic Flow by Crabs: from Eye Movements to Electrophysiology. in *The Crustacean Nervous System* (ed. Wiese, K.) 468–485 (Springer, Berlin, Heidelberg, 2002). doi:10.1007/978-3-662-04843-6_35

13. Britten, K. H. Mechanisms of Self-Motion Perception. *https://doi.org/10.1146/annurev.neuro.29.051605.112953* **31**, 389–410 (2008).

14. Hausen, K. The Lobula-Complex of the Fly: Structure, Function and Significance in Visual Behaviour. in *Photoreception and Vision in Invertebrates* 523–559 (Springer, Boston, MA, 1984). doi:10.1007/978-1-4613-2743-1_15

1333 15. Matsuda, K. & Kubo, F. Circuit Organization Underlying Optic Flow Processing
1334 in Zebrafish. *Front. Neural Circuits* **15**, 73 (2021).

1335 16. Paulk, A. C., Phillips-Portillo, J., Dacks, A. M., Fellous, J. M. & Gronenberg, W.
1336 The processing of color, motion, and stimulus timing are anatomically
1337 segregated in the bumblebee brain. *J. Neurosci.* **28**, 6319–6332 (2008).

1338 17. Rasmussen, R. N., Matsumoto, A., Arvin, S. & Yonehara, K. Binocular
1339 integration of retinal motion information underlies optic flow processing by the
1340 cortex. *Curr. Biol.* **31**, 1165-1174.e6 (2021).

1341 18. Lappe, M. *et al.* Perception of self-motion from visual flow. *Trends Cogn. Sci.*
1342 **3**, 329–336 (1999).

1343 19. Warren, J., Kay, B. A., Zosh, W. D., Duchon, A. P. & Sahuc, S. Optic flow is
1344 used to control human walking. *Nat. Neurosci. 2001 42* **4**, 213–216 (2001).

1345 20. Warren, W. H., Morris, M. W. & Kalish, M. Perception of Translational Heading
1346 From Optical Flow. *J. Exp. Psychol. Hum. Percept. Perform.* **14**, 646–660
1347 (1988).

1348 21. Angelaki, D. E. & Hess, B. J. M. Self-motion-induced eye movements: Effects
1349 on visual acuity and navigation. *Nat. Rev. Neurosci.* **6**, 966–976 (2005).

1350 22. Cullen, K. E. & Taube, J. S. Our sense of direction: Progress, controversies
1351 and challenges. *Nat. Neurosci.* **20**, 1465–1473 (2017).

1352 23. Theobald, J. Insect Flight: Navigating with Smooth Turns and Quick Saccades.
1353 *Curr. Biol.* **27**, R1125–R1127 (2017).

1354 24. Kim, A. J., Fitzgerald, J. K. & Maimon, G. Cellular evidence for efference copy
1355 in Drosophila visuomotor processing. *Nat. Neurosci.* **18**, 1247–1255 (2015).

1356 25. Fenk, L. M., Kim, A. J. & Maimon, G. Suppression of motion vision during
1357 course-changing, but not course-stabilizing, navigational turns. *Curr. Biol.* **31**,
1358 4608-4619.e3 (2021).

1359 26. Duffy, C. J. MST neurons respond to optic how and translational movement. *J.*

Neurophysiol. **80**, 1816–1827 (1998).

27. Fujiwara, T., Cruz, T. L., Bohnslav, J. P. & Chiappe, M. E. A faithful internal representation of walking movements in the Drosophila visual system. *Nat. Neurosci.* **20**, 72–81 (2017).

28. Borst, A., Haag, J. & Reiff, D. F. Fly motion vision. *Annu. Rev. Neurosci.* **33**, 49–70 (2010).

29. Farrow, K., Haag, J. & Borst, A. Nonlinear, binocular interactions underlying flow field selectivity of a motion-sensitive neuron. *Nat. Neurosci.* **9**, 1312–1320 (2006).

30. Pokusaeva, V. O., Satapathy, R., Symonova, O. & Jösch, M. Gap junctions arbitrate binocular course control in flies. *bioRxiv* 2023.05.31.543181 (2023). doi:10.1101/2023.05.31.543181

31. Haag, J. & Borst, A. Orientation tuning of motion-sensitive neurons shaped by vertical-horizontal network interactions. *J. Comp. Physiol. A Neuroethol. Sensory, Neural, Behav. Physiol.* **189**, 363–370 (2003).

32. Schnell, B. *et al.* Processing of horizontal optic flow in three visual interneurons of the Drosophila brain. *J. Neurophysiol.* **103**, 1646–1657 (2010).

33. Cruz, T. *et al.* Motor context coordinates visually guided walking in Drosophila. *bioRxiv* 1–49 (2019). doi:10.1101/572792

34. Zhao, A. *et al.* Eye structure shapes neuron function in Drosophila motion vision. *bioRxiv* 2022.12.14.520178 (2022).

35. Busch, C., Borst, A. & Mauss, A. S. Bi-directional Control of Walking Behavior by Horizontal Optic Flow Sensors. *Curr. Biol.* **28**, 4037-4045.e5 (2018).

36. Fujiwara, T., Brotas, M. & Chiappe, M. E. Walking strides direct rapid and flexible recruitment of visual circuits for course control in Drosophila. *Neuron* **110**, 2124-2138.e8 (2022).

37. Suver, M. P., Huda, A., Iwasaki, N., Safarik, S. & Dickinson, M. H. An array of

1387 descending visual interneurons encoding self-motion in Drosophila. *J.*
1388 *Neurosci.* **36**, 11768–11780 (2016).

1389 38. Namiki, S., Dickinson, M. H., Wong, A. M., Korff, W. & Card, G. M. The
1390 functional organization of descending sensory-motor pathways in drosophila.
1391 *Elife* **7**, (2018).

1392 39. Cruz, T. L., Pérez, S. M. & Chiappe, M. E. Fast tuning of posture control by
1393 visual feedback underlies gaze stabilization in walking Drosophila. *Curr. Biol.*
1394 **31**, 4596–4607 (2021).

1395 40. Zheng, Z. *et al.* A Complete Electron Microscopy Volume of the Brain of Adult
1396 Drosophila melanogaster. *Cell* **174**, 730-743.e22 (2018).

1397 41. Dorkenwald, S. *et al.* FlyWire: Online community for whole-brain
1398 connectomics. *bioRxiv* 2020.08.30.274225 (2020).
1399 doi:10.1101/2020.08.30.274225

1400 42. Scheffer, L. K. *et al.* A connectome and analysis of the adult drosophila central
1401 brain. *Elife* **9**, 1–74 (2020).

1402 43. Hengstenberg, R. Gaze control in the blowfly Calliphora: a multisensory, two-
1403 stage integration process. *Semin. Neurosci.* **3**, 19–29 (1991).

1404 44. Parsons, M. M., Krapp, H. G. & Laughlin, S. B. A motion-sensitive neurone
1405 responds to signals from the two visual systems of the blowfly, the compound
1406 eyes and ocelli. *J. Exp. Biol.* **209**, 4464–4474 (2006).

1407 45. Eckert, H. & Dvorak, D. R. The centrifugal horizontal cells in the lobula plate of
1408 the blowfly, Phaenicia sericata. *J. Insect Physiol.* **29**, 547–560 (1983).

1409 46. Wei, H., Kyung, H. Y., Kim, P. J. & Desplan, C. The diversity of lobula plate
1410 tangential cells (LPTCs) in the Drosophila motion vision system. *J. Comp.*
1411 *Physiol. A Neuroethol. Sensory, Neural, Behav. Physiol.* **206**, 139–148 (2020).

1412 47. Rayshubskiy, A. *et al.* Neural control of steering in walking Drosophila. *bioRxiv*
1413 2020.04.04.024703 (2020).

1414 48. Namiki, S. & Kanzaki, R. Brain Premotor Centers for Pheromone Orientation
1415 Behavior. 243–264 (2020). doi:10.1007/978-981-15-3082-1_12

1416 49. Namiki, S., Wada, S. & Kanzaki, R. Descending neurons from the lateral
1417 accessory lobe and posterior slope in the brain of the silkmoth Bombyx mori.
1418 *Sci. Reports 2018 81* **8**, 1–19 (2018).

1419 50. Kim, A. J., Fenk, L. M., Lyu, C. & Maimon, G. Quantitative Predictions
1420 Orchestrate Visual Signaling in Drosophila. *Cell* **168**, 280-294.e12 (2017).

1421 51. Fischer, P. J. & Schnell, B. Multiple mechanisms mediate the suppression of
1422 motion vision during escape maneuvers in flying Drosophila. *iScience* **25**,
1423 105143 (2022).

1424 52. Eckstein, N. *et al.* Neurotransmitter classification from electron microscopy
1425 images at synaptic sites in Drosophila. *bioRxiv* (2020).
1426 doi:10.1101/2020.06.12.148775

1427 53. Fisher, Y. E. *et al.* FlpStop, a tool for conditional gene control in Drosophila.
1428 *Elife* **6**, (2017).

1429 54. Ffrench-Constant, R. H., Roush, R. T., Mortlock, D. & Dively, G. P. Isolation of
1430 Dieldrin Resistance from Field Populations of Drosophila melanogaster
1431 (Diptera: Drosophilidae). *J. Econ. Entomol.* **83**, 1733–1737 (1990).

1432 55. Ffrench-Constant, R. H., Rocheleau, T. A., Steichen, J. C. & Chalmers, A. E. A
1433 point mutation in a Drosophila GABA receptor confers insecticide resistance.
1434 *Nat. 1993 3636428* **363**, 449–451 (1993).

1435 56. Hosie, A. M., Aronstein, K., Sattelle, D. B. & Ffrench-Constant, R. H. Molecular
1436 biology of insect neuronal GABA receptors. *Trends Neurosci.* **20**, 578–583
1437 (1997).

1438 57. Haag, J., Wertz, A. & Borst, A. Central gating of fly optomotor response. *Proc.*
1439 *Natl. Acad. Sci. U. S. A.* **107**, 20104–20109 (2010).

1440 58. Wertz, A., Haag, J. & Borst, A. Local and global motion preferences in
1441 descending neurons of the fly. *J. Comp. Physiol. A. Neuroethol. Sens. Neural.*

1442 *Behav. Physiol.* **195**, 1107–1120 (2009).

1443 59. Wertz, A., Haag, J. & Borst, A. Integration of binocular optic flow in cervical
1444 neck motor neurons of the fly. *J. Comp. Physiol. A Neuroethol. Sensory,*
1445 *Neural, Behav. Physiol.* **198**, 655–668 (2012).

1446 60. Strausfeld, N. J., Seyan, H. S. & Milde, J. J. The neck motor system of the fly
1447 Calliphora erythrocephala - I. Muscles and motor neurons. *J. Comp. Physiol. A*
1448 **160**, 205–224 (1987).

1449 61. Huston, S. J. & Krapp, H. G. Visuomotor Transformation in the Fly Gaze
1450 Stabilization System. *PLOS Biol.* **6**, e173 (2008).

1451 62. Haag, J., Wertz, A. & Borst, A. Integration of Lobula Plate Output Signals by
1452 DNOVS1, an Identified Premotor Descending Neuron. *J. Neurosci.* **27**, 1992–
1453 2000 (2007).

1454 63. Strausfeld, N. J. & Bassemir, U. K. Lobula plate and ocellar interneurons
1455 converge onto a cluster of descending neurons leading to neck and leg motor
1456 neuropil in Calliphora erythrocephala. *Cell Tissue Res.* **240**, 617–640 (1985).

1457 64. Kress, D. & Egelhaaf, M. Head and body stabilization in blowflies walking on
1458 differently structured substrates. *J. Exp. Biol.* **215**, 1523–1532 (2012).

1459 65. Schilstra, C. & Van Hateren, J. H. Stabilizing gaze in flying blowflies. *Nat. 1998*
1460 *3956703* **395**, 654–654 (1998).

1461 66. Seelig, J. D. & Jayaraman, V. Neural dynamics for landmark orientation and
1462 angular path integration. *Nat. 2015 5217551* **521**, 186–191 (2015).

1463 67. Green, J. *et al.* A neural circuit architecture for angular integration in
1464 Drosophila. *Nat. 2017 5467656* **546**, 101–106 (2017).

1465 68. Turner-Evans, D. B. *et al.* The Neuroanatomical Ultrastructure and Function of
1466 a Biological Ring Attractor. *Neuron* **108**, 145-163.e10 (2020).

1467 69. Fisher, Y. E., Marquis, M., D'Alessandro, I. & Wilson, R. I. Dopamine promotes
1468 head direction plasticity during orienting movements. *Nat. 2022 6127939* **612**,

1469 316–322 (2022).

1470 70. Mauss, A. S. *et al.* Neural Circuit to Integrate Opposing Motions in the Visual
1471 Field. *Cell* **162**, 351–362 (2015).

1472 71. Braun, A., Borst, A. & Meier, M. Disynaptic inhibition shapes tuning of OFF-
1473 motion detectors in Drosophila. *Curr. Biol.* **33**, 2260-2269.e4 (2023).

1474 72. Kress, D. & Egelhaaf, M. Gaze characteristics of freely walking blowflies
1475 Calliphora vicina in a goal-directed task. *J. Exp. Biol.* **217**, 3209–3220 (2014).

1476 73. Koyama, M. *et al.* A circuit motif in the zebrafish hindbrain for a two alternative
1477 behavioral choice to turn left or right. *Elife* **5**, (2016).

1478 74. Essig, J., Hunt, J. B. & Felsen, G. Inhibitory neurons in the superior colliculus
1479 mediate selection of spatially-directed movements. *Commun. Biol. 2021 41* **4**,
1480 1–14 (2021).

1481 75. Haag, J. & Borst, A. Recurrent network interactions underlying flow-field
1482 selectivity of visual interneurons. *J. Neurosci.* **21**, 5685–5692 (2001).

1483 76. Silies, M., Gohl, D. M. & Clandinin, T. R. Motion-Detecting Circuits in Flies:
1484 Coming into View. (2014). doi:10.1146/annurev-neuro-071013-013931

1485 77. Borst, A. & Helmstaedter, M. Common circuit design in fly and mammalian
1486 motion vision. *Nat. Neurosci.* **18**, 1067–1076 (2015).

1487 78. Agrochao, M., Tanaka, R., Salazar-Gatzimas, E. & Clark, D. A. Mechanism for
1488 analogous illusory motion perception in flies and humans. *Proc. Natl. Acad.*
1489 *Sci. U. S. A.* **117**, 23044–23053 (2020).

1490 79. Nern, A., Pfeiffer, B. D. & Rubin, G. M. Optimized tools for multicolor
1491 stochastic labeling reveal diverse stereotyped cell arrangements in the fly
1492 visual system. *Proc. Natl. Acad. Sci. U. S. A.* **112**, E2967–E2976 (2015).

1493 80. Lyu, C., Abbott, L. F. & Maimon, G. Building an allocentric travelling direction
1494 signal via vector computation. *Nat. 2021 6017891* **601**, 92–97 (2021).

1495 81. Molina-Obando, S. *et al.* On selectivity in the drosophila visual system is a

1496 multisynaptic process involving both glutamatergic and GABAergic inhibition.
1497 *Elife* **8**, (2019).

1498 82. Asahina, K. *et al.* Tachykinin-expressing neurons control male-specific
1499 aggressive arousal in drosophila. *Cell* **156**, 221–235 (2014).

1500 83. Diao, F. *et al.* Plug-and-Play Genetic Access to Drosophila Cell Types using
1501 Exchangeable Exon Cassettes. *Cell Rep.* **10**, 1410–1421 (2015).

1502 84. Bates, A. S. *et al.* The natverse, a versatile toolbox for combining and
1503 analysing neuroanatomical data. *Elife* **9**, (2020).

1504 85. Schneider-Mizell, C. M. *et al.* Quantitative neuroanatomy for connectomics in
1505 Drosophila. *Elife* **5**, 1–36 (2016).

1506 86. Saalfeld, S., Cardona, A., Hartenstein, V. & Tomančák, P. CATMAID:
1507 Collaborative annotation toolkit for massive amounts of image data.
1508 *Bioinformatics* **25**, 1984–1986 (2009).

1509 87. Buhmann, J. *et al.* Automatic detection of synaptic partners in a whole-brain
1510 Drosophila electron microscopy data set. *Nat. Methods* **18**, 771–774 (2021).

1511 88. Bates, A. S. *et al.* Complete Connectomic Reconstruction of Olfactory
1512 Projection Neurons in the Fly Brain. *Curr. Biol.* **30**, 3183-3199.e6 (2020).

1513 89. Schlegel, P. *et al.* A consensus cell type atlas from multiple connectomes
1514 reveals principles of circuit stereotypy and variation. *bioRxiv*
1515 2023.06.27.546055 (2023). doi:10.1101/2023.06.27.546055

1516 90. Jenett, A. *et al.* A GAL4-Driver Line Resource for Drosophila Neurobiology.
1517 *Cell Rep.* **2**, 991–1001 (2012).

1518 91. Tirian, L. & Dickson, B. J. The VT GAL4, LexA, and split-GAL4 driver line
1519 collections for targeted expression in the Drosophila nervous system. *bioRxiv*
1520 198648 (2017). doi:10.1101/198648

1521 92. Meissner, G. W. *et al.* An image resource of subdivided Drosophila GAL4-
1522 driver expression patterns for neuron-level searches. *bioRxiv*

1523 2020.05.29.080473 (2020). doi:10.1101/2020.05.29.080473

1524 93. Otsuna, H., Ito, M. & Kawase, T. Color depth MIP mask search: a new tool to
1525 expedite Split-GAL4 creation. *bioRxiv* 318006 (2018). doi:10.1101/318006

1526 94. Dionne, H., Hibbard, K. L., Cavallaro, A., Kao, J. C. & Rubin, G. M. Genetic
1527 Reagents for Making Split-GAL4 Lines in Drosophila. *Genetics* **209**, 31–35
1528 (2018).

1529 95. Crickmore, M. A. & Vosshall, L. B. Opposing Dopaminergic and GABAergic
1530 Neurons Control the Duration and Persistence of Copulation in Drosophila.
1531 *Cell* **155**, 881–893 (2013).

1532 96. Reiser, M. B. & Dickinson, M. H. A modular display system for insect
1533 behavioral neuroscience. *J. Neurosci. Methods* **167**, 127–139 (2008).

1534 97. Weir, P. T. & Dickinson, M. H. Functional divisions for visual processing in the
1535 central brain of flying Drosophila. *Proc. Natl. Acad. Sci. U. S. A.* **112**, E5523–
1536 E5532 (2015).

1537 98. Dana, H. *et al.* High-performance calcium sensors for imaging activity in
1538 neuronal populations and microcompartments. *Nat. Methods* **16**, 649–657
1539 (2019).

1540 99. Chen, T. W. *et al.* Ultrasensitive fluorescent proteins for imaging neuronal
1541 activity. *Nat. 2013 4997458* **499**, 295–300 (2013).

1542 100. Thurman, S. T., Guizar-Sicairos, M. & Fienup, J. R. Efficient subpixel image
1543 registration algorithms. *Opt. Lett. Vol. 33, Issue 2, pp. 156-158* **33**, 156–158
1544 (2008).

1545 101. Eichner, H., Joesch, M., Schnell, B., Reiff, D. F. & Borst, A. Internal Structure
1546 of the Fly Elementary Motion Detector. *Neuron* **70**, 1155–1164 (2011).

1547 102. Costa, M., Manton, J. D., Ostrovsky, A. D., Prohaska, S. & Jefferis, G. S. X. E.
1548 NBLAST: Rapid, Sensitive Comparison of Neuronal Structure and
1549 Construction of Neuron Family Databases. *Neuron* **91**, 293–311 (2016).

1550 103. Hulse, B. K. *et al.* A connectome of the drosophila central complex reveals
1551 network motifs suitable for flexible navigation and context-dependent action
1552 selection. *Elife* **10**, (2021).

1553 104. Vanwalleghem, G., Constantin, L. & Scott, E. K. Calcium Imaging and the
1554 Curse of Negativity. *Front. Neural Circuits* **14**, 607391 (2021).

1555

1556

1557

Figure 1: DNp15 exhibit enhanced sensitivity to rotational optic flow compared to HS cells and plays a role in steering during high-speed translation

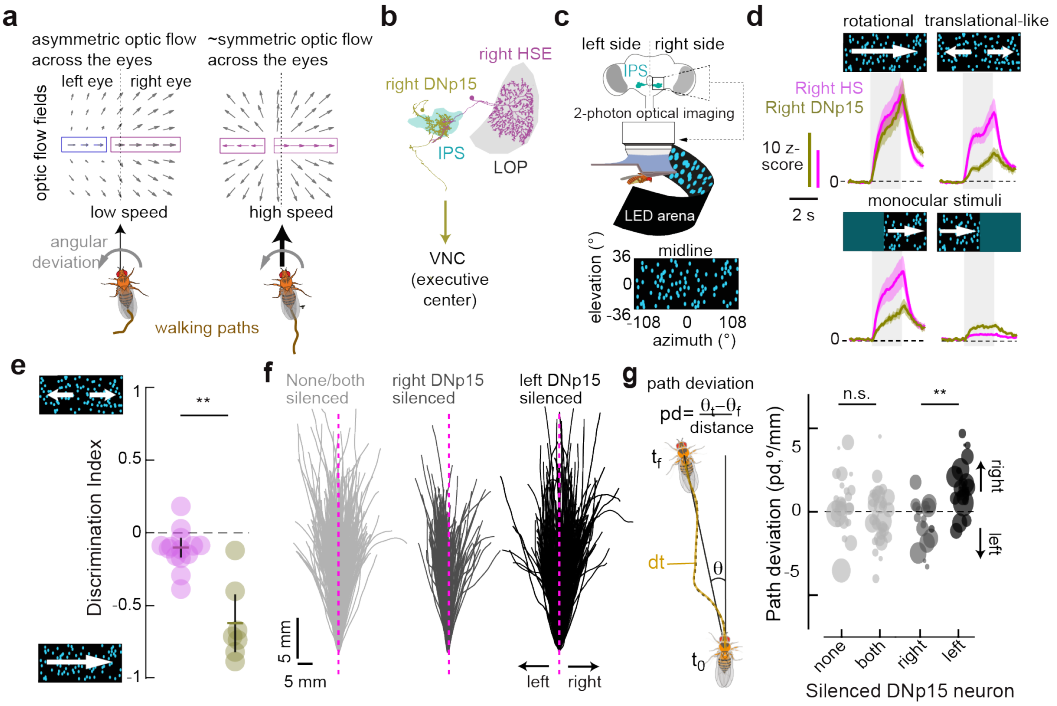

Figure 1: DNp15 exhibit enhanced sensitivity to rotational optic flow compared to HS and plays a role in steering during high-speed translation (**a**) Simulated binocular optic flow of a fly walking at low (left) versus high (right) forward speed and rotating with the same angular velocity. Rectangles indicate the presence of regressive (blue) or progressive (magenta) motion detected by a horizontal motion-sensitive system. (**b**) EM-reconstructed right HS (magenta) and postsynaptic right DNp15 (olive) cells. The chemical and electrical synapses between the two cells allocated within the inferior posterior slope (IPS, cyan), a premotor region. The dendrites of HS cells are located within the lobula plate (LOP). (**c**) Top, schematic of the fly brain and the IPS, where optical imaging was performed. Bottom, 2-photon calcium imaging setup and the visual LED display. (**d**) HS (magenta) and DNp15 (olive) calcium responses to horizontal binocular rotational or translational-like optic flow (top), and to monocular stimuli (bottom). (**e**) Discrimination index (see **Methods**) between translational-like and rotational stimuli in HS (magenta) and DNp15 (olive). Each circle represents an individual ROI. Colored horizontal line and black vertical line represent the mean and 95% CI. (HS: N=12 flies, n=16 ROIs, DNp15: N=6 flies n=7 ROIs, *P < 0.05; **P < 0.01 ***P < 0.001, Wilcoxon's rank-sum test). (**f**) The walking paths of forward runs of length ≥ 4 body lengths, aligned at their origin, in flies with either both or none DNP15 silenced (left, light gray traces), right DNp15 silenced (middle, gray traces), and left DNP15 silenced (right, black traces). (**g**) Left, definition of path deviation, the difference in body orientation between the end and the beginning of the walking path over traveled distance. Right, mean path deviation from per fly in flies with none, single or both DNp15 silenced. The size of the circle indicates the number of walking bouts per fly, with larger sizes representing larger number of walking bouts. Number of flies per condition, none n=25; both n=31; left n=22; right n=22; $*p < 0.05$ $**p < 0.01$ $***p < 0.001$, Wilcoxon's rank-sum test with Bonferroni correction for multiple comparisons.)

1558

Figure 2: H2, HS and VS cells form two distinctive networks in the central brain

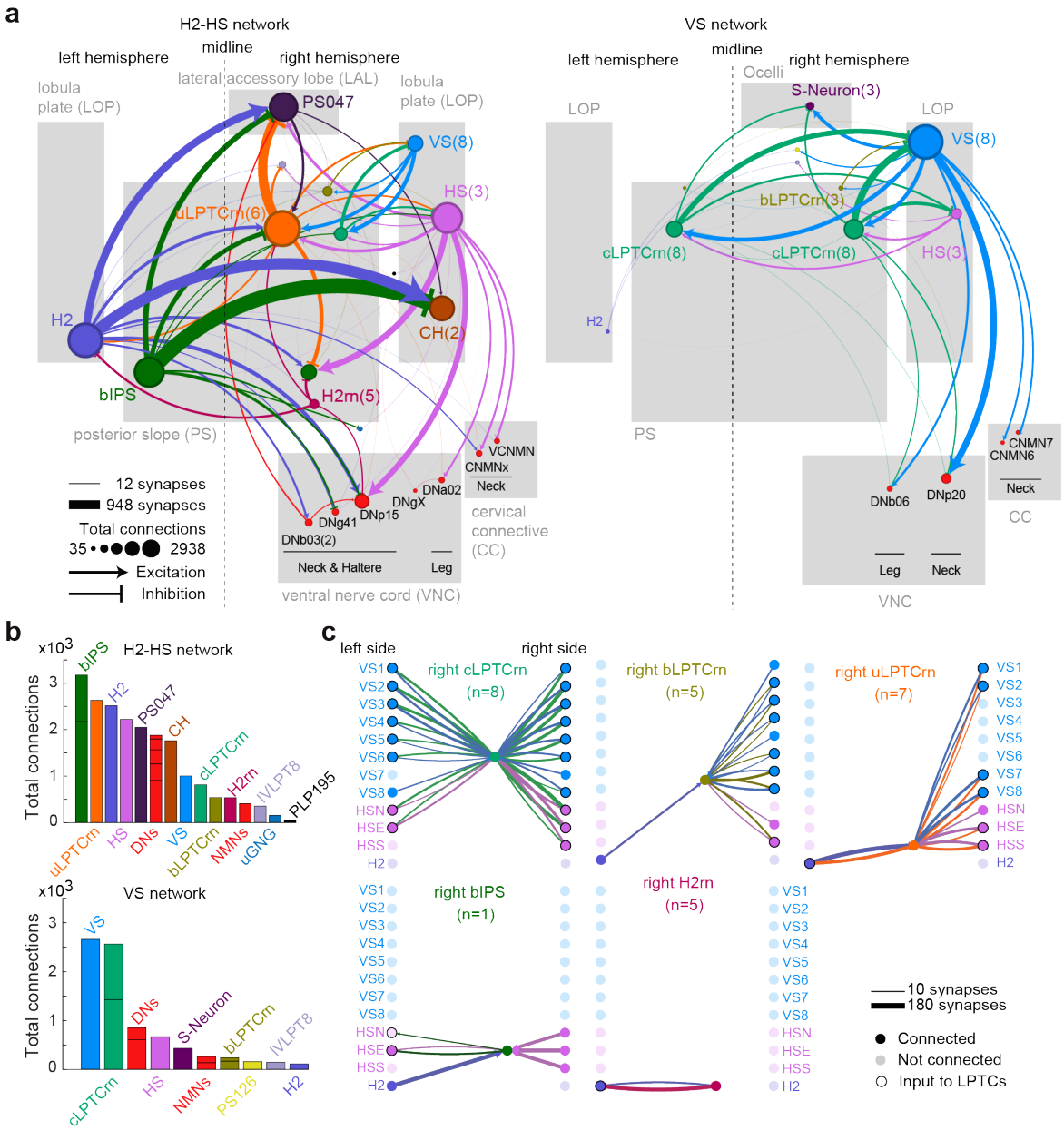

Figure 2. H2, HS and VS cells form two distinctive networks in the central brain. (**a**) Connectivity graph of the H2-HS (left) and VS (right) networks. Neurons are represented as nodes (circles), with their synaptic connections indicated by arrows (predicted to be excitatory) or tee-shaped edges (predicted to be inhibitory). Thickness of the arrows/tee-shaped edges represents number of synapses, and color indicates the presynaptic neuron. For clarity, connections with fewer than 10 synapses are not shown; connections with fewer than 50 synapses are shaded. Node diameters represent the total number of connections that each node has within the network (including both inputs and outputs). Except for LPTCs, nodes are placed within the brain regions (grey rectangles) where their axons reside. (**b**) The total number of synaptic connections for each neuron within H2-HS network (Top), and VS network (bottom). See **Supplementary Table 2** for the complete list of neurons and nomenclature. (**c**) Connectivity graph between each LPTC input cell type and individual HS, H2 and VS cells. Edges indicate synaptic connection between cells, with thickness indicating number of synapses and color indicating the presynaptic cell. LPTCs without input are

Figure 3: Binocular interactions define optic flow sensitivity within the H2-HS network

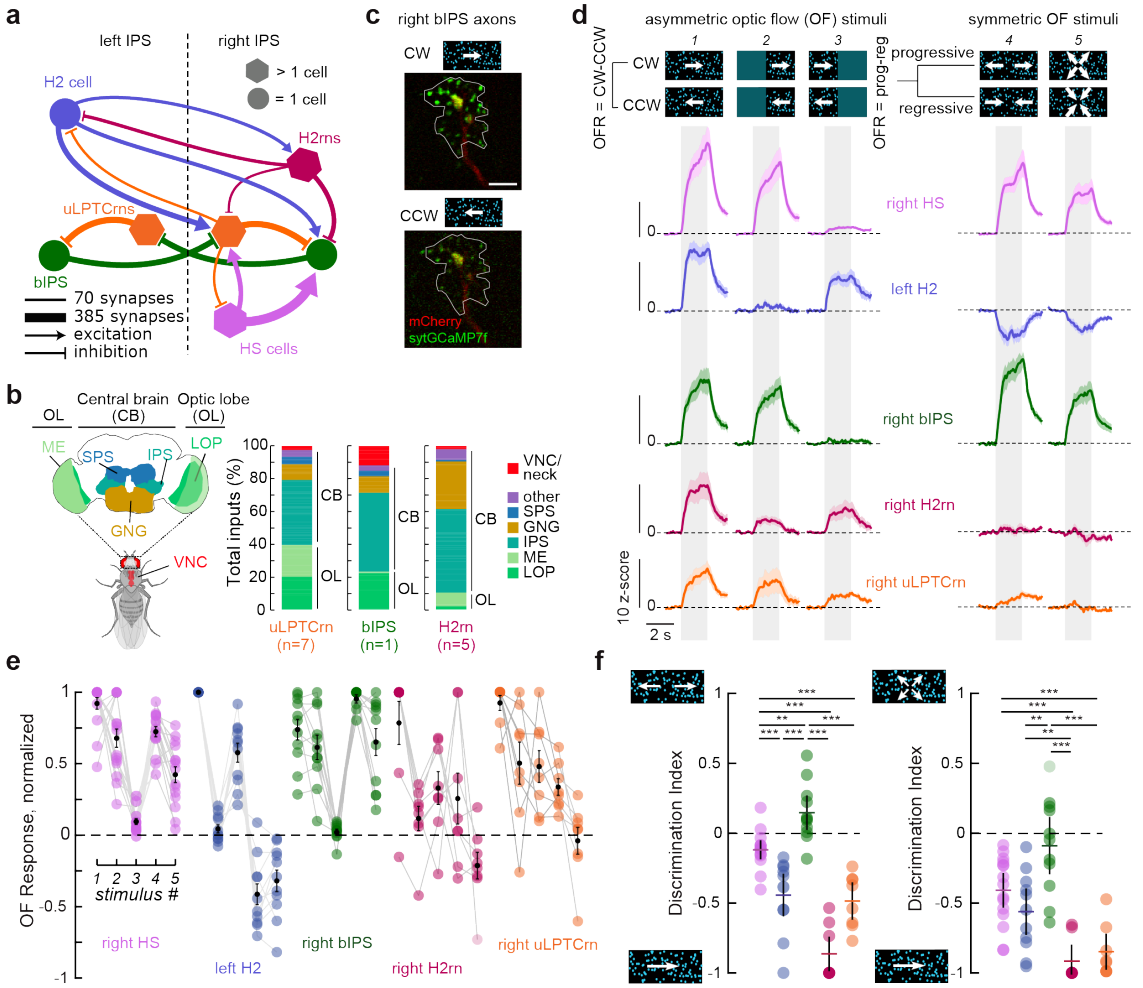

Figure 3: Binocular interactions define optic flow sensitivity within the H2-HS network. (**a**) Local connectivity between the input and middle layers of the H2-HS network. (**b**) Left, schematic of the central nervous system (CNS) regions from which uLPTCrns, bIPS and H2rns receive inputs. LOP, lobula plate; ME, medulla; GNG, gnathal ganglia; IPS, inferior poste-rior slope; SPS, superior posterior slope. Right, proportion of inputs per CNS region (color code) for each interneuron. (**c**) Single plane fluorescence image of an example recording from bIPS axons during binocular CW (top) and CCW (bottom) horizontal motion. We defined a single region of interest (ROI), which covers the entire axon is outlined in white. The red signal corresponds to mCherry fluorescence, whereas the green signal corresponds to sytGCaMP7f fluorescence. Scale bar, 10 µm. (**d**) Top: visual stimuli presented to the fly, with direction of motion as indicated by arrows. Bottom: optic flow calcium responses (OFR) of each neuron to rotational (stimuli *1, 2, 3*) or translational (stimuli *4, 5*) optic flow. OFR for rotational stimuli is defined as CW (rightwards) minus CCW (leftwards) direction of visual motion. For the translational stimuli, OFR is defined as progressive minus regressive direction of visual motion. Each trace corresponds to the grand mean of the z-scored calcium response across flies ± SEM (shade). Per fly, we obtained mean responses to 5-10 repetitions per stimulus. Light-gray rectangles indicate the stimulation window. For this and the remaining panels: HS: N=12 flies n=16 ROIs, H2: N =8 flies n=11 ROIs, bIPS: N=10 flies n=11 ROIs, H2rn: N=5 flies n=8 ROIs, uLPTCrn: N=6 flies n=8 ROIs. (**e**) Normalized OFRs (relative to the preferred stimulus per neuron). Error bars represent SEM of the grand mean across flies. (**f**) Left, discrimination index between translation-like vs. rotational stimuli (see **Methods**). Each circle represents an individual ROI. The horizontal line and black vertical line represent mean and 95% CI. Right, discrimination index between translation vs. rotational stimuli. *: $p < 0.05$; **$p < 0.01$; ***$p < 0.001$, Wilcoxon's rank-sum test with Bonferroni correction for multiple comparisons.

1561

Figure 4: GABAergic inhibition fine-tunes optic flow responses in bIPS

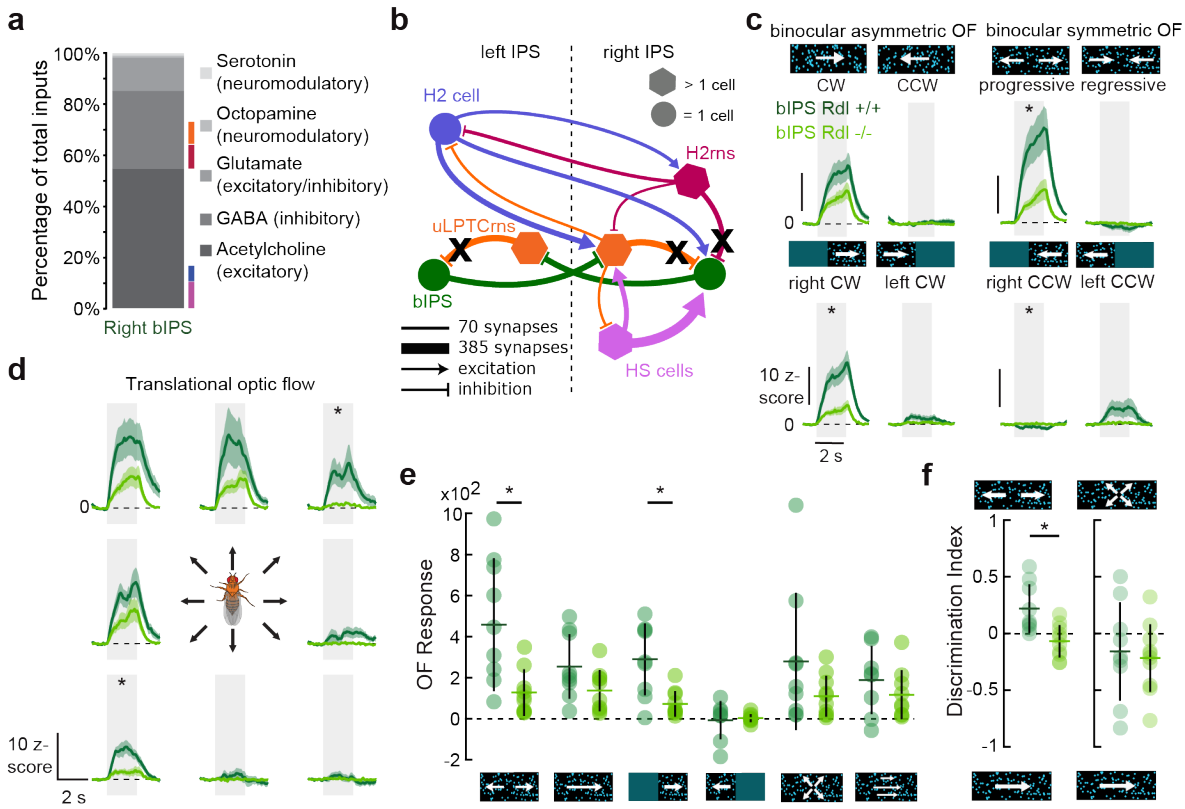

Figure 4: GABAergic inhibition fine-tunes optic flow responses in bIPS. (**a**) Right bIPS input profile, grouped by their predicted primary neurotransmitter. Neurons shown in **b**) are highlighted with colored lines. (**b**) Schematic of the local connectivity of the input and middle layers of the H2-HS network. Inhibitory connections are shown as tee shaped edges. Blocking Rdl receptors in bIPS using FLPStop disrupts fast GABAergic signaling onto bIPS (black crosses). (**c**) Neural responses of wild type (dark green) and Rdl-disrupted (light green) bIPS cells to binocular asymmetric (left, rotational) and symmetric (right, translational-like) optic flow (OF). Each trace corresponds to the grand mean ± SEM (shaded area) of z-scored calcium responses obtained across flies. For each fly, mean responses to 5-10 repetitions per stimulus were obtained from a single ROI at the axon terminals. Stimuli with a star indicate area under the curve (auc) responses that are statistically different from wild-type bIPS recordings. (**d**) Same as **c**), but for translational optic flow. (**e**) OF responses, the difference between the preferred and nulled direction responses (auc) for horizontal and progressive visual motion. (**f**) Left, discrimination index between translational-like and rotational optic flow of recorded neurons in **c**) (see **Methods**). Each circle represents an individual ROI. Colored horizontal line and black vertical line represents mean and 95% CI. Right, discrimination index between progressive and rotational optic flow. For all panels: bIPS: N=7 flies n=9 ROIs, bIPS Rdl-FLPStop: N=7 flies n=10 ROIs. *P < 0.05; **P < 0.01 ***P < 0.001, Wilcoxon's rank-sum test.

1562

1563

Figure 5: A lateral disinhibitory motif enhance asymmetries in neural activity across the right versus left hemisphere

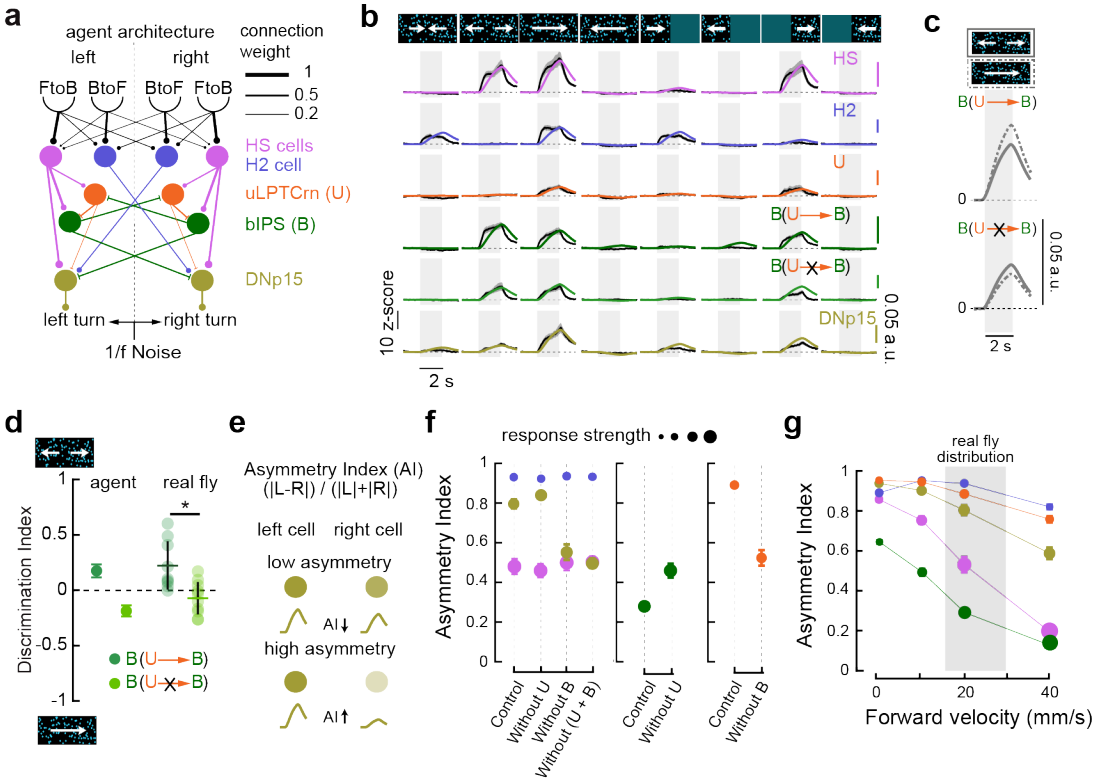

Figure 5: A lateral disinhibitory motif enhance asymmetries in neural activity across the right versus left hemisphere. (**a**) Schematic of the agent architecture: two sets of Reichardt detectors tuned to front-to-back (FtoB) or back-to-front (BtoF) motion detect the optic flow generated by a simulated walking fly (See **Methods**, **Fig. 5-S1**). The detected visual motion is processed by a network of nodes that mimic the core network motif of H2-HS network (**Fig. 3a**). The weights that connect the nodes are tuned based on a subset of measured visual responses (**Fig. 5-S1**). (**b**) Simulated and observed visual responses to monocular and binocular patterns of optic flow. Responses were matched to the maximal observed response. Observed responses are replotted from **Fig. 3-S2** and **Fig. 4c** (**c**) Visual response of modeled bIPS to symmetric or asymmetric binocular optic flow, and with or without a functional input from uLPTCrns. (**d**) Left: discrimination index of modeled and observed bIPS with or without a functional input from uLPTCrns. Right: observed bIPS' discrimination index with or without functional GABAergic input (replotted from **Fig. 4f**). (**e**) Definition of the Asymmetry Index (AI) and two example conditions with low and high AI values. (**f**) Asymmetry index of simulated neurons (colored) in the full model (Control), under bIPS silencing (Without B), under uLPTCrn silencing (Without U) and under both bIPS and uLPTCrn silencing (Without U+B). The dot size corresponds to the magnitude of the neural response. (**g**) Asymmetry index of simulated neurons (colored) in the full model varying the forward velocity of the agent. The shaded area corresponds to the range of velocities observed for forward runs in real exploratory flies (Cruz et al. 2021).

Figure 6: bIPS plays a role in steering control during high-speed walking

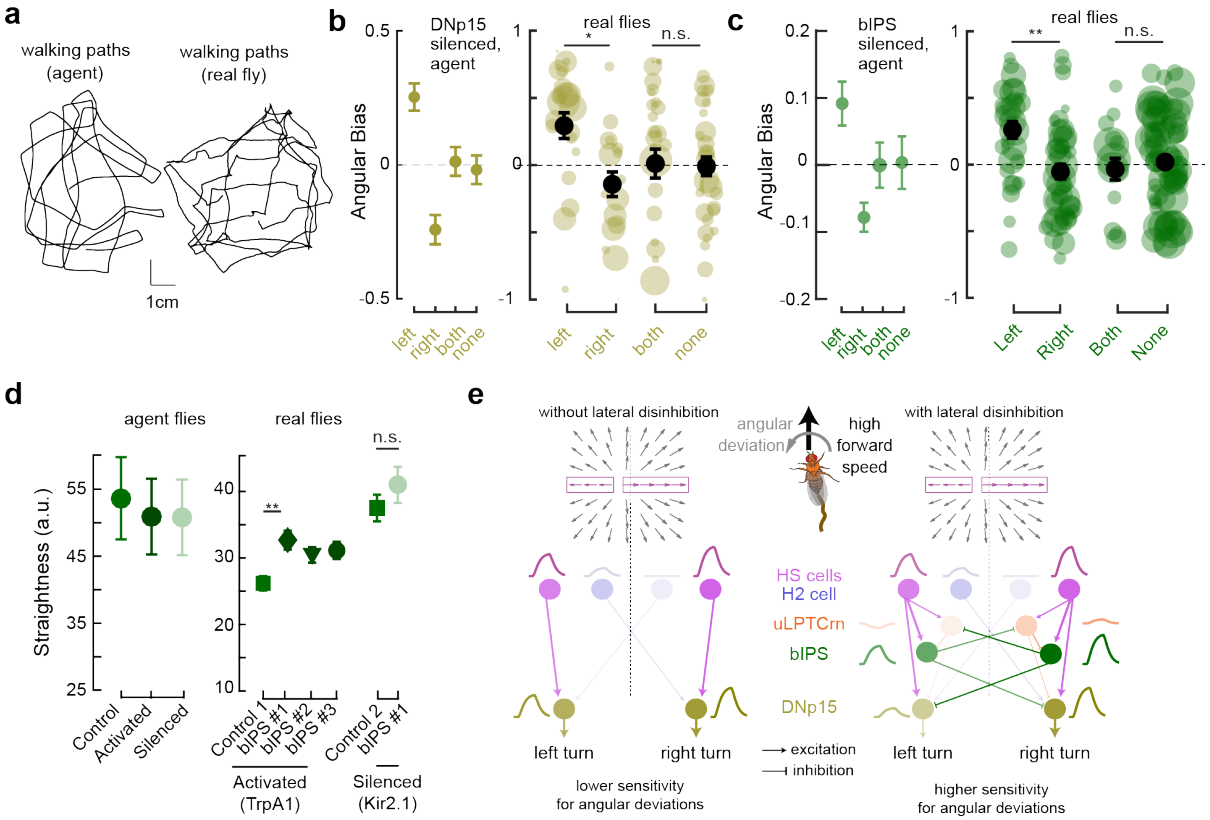

Figure 6: bIPS plays a role in steering control during high-speed walking. (**a**) Example walking paths of the agent (left) and the real fly (right) under prominent visual feedback. (**b**) Simulated (left) and real fly (right) angular bias during forward runs (see **Methods**) with DNp15 activity perturbed bilateral or unilaterally. Transparent dots depict mean bias of individual flies, black dots represent grand mean per genotype, weighted by the amount of walking bouts (dot size). Error bars represent SEM. Number of flies per condition, none n=25; left n=22; right n=22; both n=31. (**c**) Same as **b**), but for bIPS. Number of flies per condition, none n=65; left n=26; right n=38; both n=13. For (**b**) and (**c**): *p < 0.05; **p < 0.01 ***p < 0.001, Wilcoxon's rank-sum test with Bonferroni correction for multiple comparisons. (**d**) Left, simulated straightness of the agent during forward runs (see **Methods**) with control (green), bilaterally activated (dark green) or silenced (light green) bIPS cells. Right, straigtness of control flies (green), or flies with bilaterally activated (dark green) or silenced (light green) bIPS cells. Number of flies per condition, empty control>TrpA1 n=25; bIPS#1>TrpA1 n=27; bIPS#2>TrpA1 n=25; bIPS#3>Tr-pA1 n=29; empty control>Kir2.1 n=22; bIPS#1>Kir2.1 n=23. (**e**) Summary of the findings. The middle layer of the H2-HS network supports steering by enhancing the difference in the activity levels of the output layer across hemispheres. This function is driven by a competitive disinhibitory motif that is well posed to be recruited at high-speed walking. In this condition, binocular optic flow may contain prominent translational components, possibly overshadowing rotational cues that are critical for course control. We propose that the competitive disinhibition at the middle layer plays an important role in modulating the output layer in a continuous and dynamic manner, leading to a more robust estimate of the deviations from a straight course.